

ALMA Mater Studiorum
Università degli Studi di Bologna

SCUOLA DI SCIENZE

Corso di Laurea Magistrale in Astrofisica e Cosmologia

Dipartimento di Fisica e Astronomia

Constraining mass and shape of galaxy clusters
through large scale structures

Elaborato Finale

Candidato:

Elena Sacchi

Relatore:

Chiar.mo Prof.:

Lauro Moscardini

Co-relatore:

Steen H. Hansen

Sessione II
Anno Accademico 2013/14

Φύσις κρύπτεσθαι φιλεῖ.
Nature aims to remain a mystery.
La Natura mira a rimanere un mistero.
(Eraclito)

Sommario

L'osservazione dell'Universo su grande scala mostra che la materia forma un sistema complesso, spesso chiamato *ragnatela cosmica* (cosmic web), contenente strutture disomogenee, come ammassi, strutture planari e filamentari, circondate da grandi vuoti. Lo stesso scenario emerge da simulazioni cosmologiche della distribuzione di materia oscura.

Questo tipo di aggregazione è profondamente connesso con il processo di formazione delle strutture, in cui le strutture cosmiche risultano dalla crescita e successiva aggregazione di piccole fluttuazioni iniziali di densità nell'Universo primordiale. Il processo di accrescimento comporta che la materia collassi in strutture planari e filamentari e si aggrega per formare gli ammassi. Gli ammassi di galassie sono quindi collocati all'intersezione di questi filamenti e la loro parte più interna tende alla fine a raggiungere l'equilibrio dinamico.

Come risultato di questo collasso gravitazionale, chiamato aggregazione gerarchica, gli ammassi di galassie, gli oggetti più grandi gravitazionalmente legati che osserviamo, dovrebbero essere le strutture formatesi più di recente nell'Universo. Anche per questo motivo sono uno strumento fondamentale per la determinazione dei parametri cosmologici che descrivono il contenuto di materia ed energia dell'Universo e per lo studio del processo di formazione delle strutture.

In particolare, la determinazione della loro massa è un punto cruciale per un ramo dell'astrofisica chiamato *Cosmologia*, che studia le proprietà dell'Universo su grandissima scala, la sua nascita e la sua evoluzione.

La misura della massa di un ammasso di galassie può essere ottenuta in diversi modi, che sfruttano la grande varietà di componenti contenute in questi oggetti: galassie e quindi stelle, gas caldo diffuso e materia oscura. Tuttavia, ognuno di questi metodi si basa su forti assunzioni riguardo lo stato dinamico o idrodinamico dell'ammasso (ad esempio equilibrio viriale o equilibrio idrostatico), oppure sulla sua geometria, solitamente assunta sferica.

Lo scopo di questa Tesi è la descrizione di un nuovo metodo per la misura della massa degli ammassi di galassie che utilizza unicamente informazioni cinematiche di strutture al di fuori dell'ammasso, dove la materia non ha ancora raggiunto l'equilibrio. Questo metodo parte dall'identificazione di gruppi di galassie distribuite in strutture planari o filamentari ed arriva alla massa dell'ammasso di galassie modellando quanto l'ammasso stesso perturba il loro moto dal semplice *flusso di Hubble* (Hubble flow), ovvero la loro partecipazione all'espansione dell'Universo. L'identificazione delle strutture avviene nello spazio delle fasi, ovvero il piano formato dal raggio proiettato sul piano del cielo e dalla velocità lungo la linea di vista delle galassie nei dintorni dell'ammasso. Una volta trovata una sovradensità in questo spazio, il modellamento del suo profilo di velocità si basa su di un metodo Monte Carlo che richiede in input le coordinate in tale spazio delle fasi delle galassie all'interno del filamento, e restituisce la massa dell'ammasso e l'orientamento tridimensionale della struttura trovata. Questo metodo non richiede l'analisi dinamica della regione virializzata dell'ammasso e quindi non è basato su nessuna ipotesi sul suo stato dinamico. Tuttavia nell'assunzione di un profilo di velocità radiale viene implicitamente assunta la simmetria sferica dell'ammasso.

Il metodo è stato testato dapprima su simulazioni cosmologiche (capitolo 4) e poi sull'ammasso di Coma, Abell 1656 (capitolo 5).

Per ogni oggetto analizzato sono state trovate diverse strutture, che danno ognuna un risultato leggermente diverso per la massa dell'ammasso. Queste differenze sono state usate per provare a riprodurre l'orientamento e la forma tridimensionale dell'ammasso, in quanto strutture situate lungo assi diversi dell'oggetto centrale dovrebbero sentire un potenziale gravitazionale differente se l'ammasso non è sferico. Ad esempio, un filamento lungo l'asse maggiore sente un potenziale più grande (ed uno posto lungo l'asse minore più piccolo) di quello aspettato, e questo porta ad una sovra-stima (o sotto-stima) della massa reale. Combinando le misure di massa restituite da filamenti diversi si dovrebbe quindi poter dedurre la forma dell'ammasso, ed in effetti sono state trovate delle prime indicazioni qualitative di questo effetto (capitolo 6).

Contents

1	Introduction	1
1.1	Large scale Universe	4
1.2	Composition of the Universe	5
1.3	Structure Formation	8
1.4	Galaxy clusters	9
1.5	Clusters and Cosmology	10
2	Mass estimation of galaxy clusters	13
2.1	Mass from virial theorem	14
2.2	Mass from Jeans equation	15
2.3	Mass from hot gas emission	16
2.4	Mass from gravitational lensing	19
2.5	Mass from Sunyaev-Zel'dovich effect	24
2.6	Mass from caustic technique	26
3	A new method to measure the mass of galaxy clusters	29
3.1	Radial infall velocity profile	30
3.2	Identification of filaments and sheets	33
3.2.1	Cells	33
3.2.2	Rectangles	36
3.3	Mass and orientation	39
4	Results on cosmological simulation	41
4.1	Halo 29	43
4.2	Halo 30	51
4.3	Halo 42	54
4.4	Halo 50	57
4.5	Discussion	59
5	Results on Coma cluster	63
5.1	The sample	65

5.2	Identification of the sheets	66
5.3	Analysis and results	68
6	Shape and alignment of galaxy clusters	71
6.1	Effect of asphericity	72
6.2	Combining different data sets	74
6.3	Considerations on the “sheets method”	76
6.3.1	Looking at simulated halos in 3D	77
6.3.2	Color maps	79
7	Conclusions	83
	Bibliography	91

Chapter 1

Introduction

The technological improvement occurred over the last century allowed us to explore ever deeper the Universe and to study its large scale structure. This led to the development of a branch of astrophysics called Cosmology, whose main purpose is the study of the Universe as a whole and of the laws that rule its origin, evolution and fate.

The first drive to the origin of the so-called modern Cosmology was the discovery of the expansion of the Universe, made by Edwin P. Hubble in 1929. He observed that all the galaxies are receding from us and from each other, so the light coming from a galaxy should arrive to us with a wavelength larger than the one originally emitted. This yielded to the definition of *redshift*, one of the most used quantities for the description of the Universe. Hubble also discovered that a linear relation exists between the distance of a galaxy and its receding velocity, the so-called Hubble law:

$$v = H_0 r,$$

where $H_0 = 100 h$ km/s/Mpc is defined Hubble constant and qualifies the expansion rate of the Universe at the present time. Constraining the value of H_0 (or h , the dimensionless form of the constant) is still an important goal in Cosmology.

Another crucial point was made in 1964, when Arno Penzias and Robert W. Wilson found an almost homogeneous radiation, later called *Cosmic Microwave Background* (CMB), existing in every direction they looked. This discovery gave a strong confirmation to the Big Bang model for the origin of the Universe, and made Cosmology a growing field in modern astrophysics.

The CMB radiation has a thermal spectrum very close to an ideal black body (see Fig. 1.1) and a measured temperature of $T_0 = 2.72548 \pm 0.00057$ K ^[21].

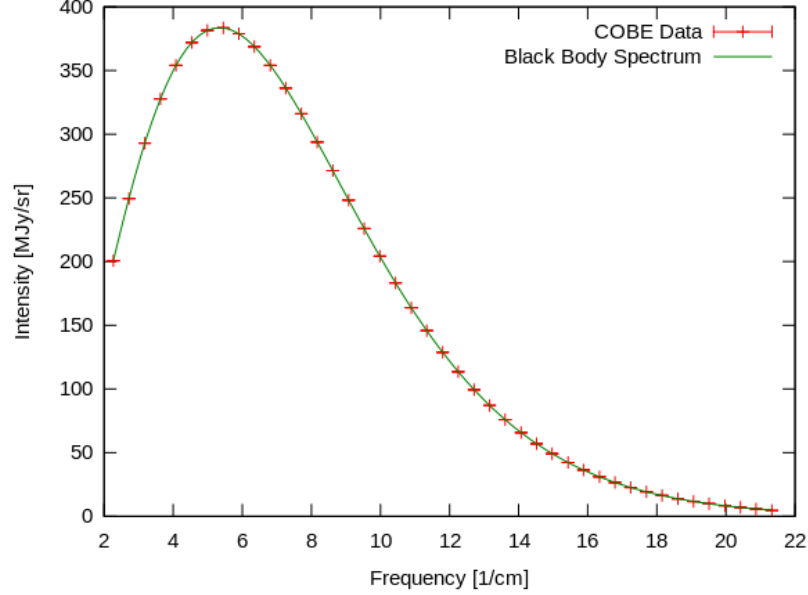


Figure 1.1: The first published spectrum of the CMB as measured by the COBE satellite in the direction of the North Galactic Pole. ^[38]

Another important property of the CMB radiation is its small temperature anisotropy, usually expressed as:

$$\frac{\Delta T}{T}(\theta, \phi) = \frac{T(\theta, \phi) - T_0}{T_0} \sim 10^{-5}$$

which gives the temperature fluctuation as a fraction of the mean temperature T_0 and as a function of angular position (θ, ϕ) on the sky. The high level of isotropy can provide important information on the origin, nature and evolution of density fluctuations which are thought to give rise to galaxies and large scale structures in the Universe.

In fact the CMB should originate in the early stages of the Universe, when matter and radiation were a hot dense plasma in thermal equilibrium thanks to the Thomson scatters between photons and electrons. With the expansion of Universe the temperature decreased, as well as the degree of ionization since atoms started forming, and the scatters became less and less effective, producing the so-called *decoupling* between matter and radiation, which hereafter start a separate evolution.

The CMB is the leftover radiation of this last scatter and should bear the imprint of the physical processes happened both during and after its production. In fact, the anisotropies observed in the CMB are thought to be the signs of the primordial fluctuations that are the seeds of galaxies and clusters.

The basic assumption on which Cosmology is grounded is the *Cosmological Principle*, at first introduced by Albert Einstein in its Relativity Theory. This “principle” states that at a given time there is a scale such that the Universe is both homogeneous and isotropic. Homogeneity is the property of being identical everywhere in space, while isotropy is the property of looking the same in every direction. The Universe is not exactly homogeneous, so this definition of homogeneity is meant in an average sense: the Universe is taken to be identical in different places when one looks at sufficiently large scales ^[14].

1.1 Large scale Universe

Despite the assumption of the Cosmological Principle, the observation of the large scale Universe shows that the matter distribution is far from isotropic. Instead there is a large variety of structures, such as clusters, sheets and filaments, as well as large void spaces (see Fig. 1.2).

This kind of inhomogeneities is seen on all scales studied so far, from galaxies to galaxy clusters, and shows the tendency of matter to concentrate from small to large scales, where “large” means scales larger than that of a galaxy.

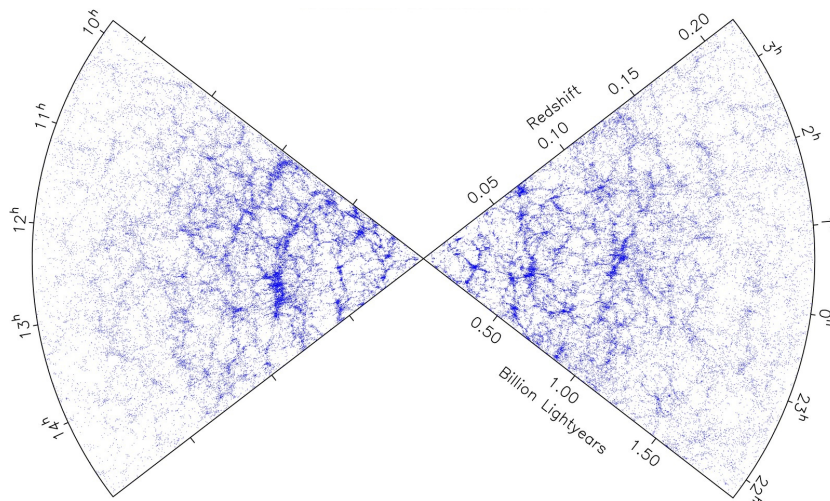


Figure 1.2: A slice of the Universe from the 2dF Galaxy Redshift Survey that maps the distribution of galaxies within a section of the sky, by combining redshift and angular position data. The figure shows the large scale structure of the Universe, with its clusters, filaments and voids. ^[15]

Among these large scale features, galaxy clusters seem to be the largest gravitationally bound structures in the Universe. The way galaxies cluster is approximately hierarchical: many galaxies occur in pairs or small groups which in turn are often clustered into larger associations ^[14]. This put galaxy clusters at the end of the structure formation process as the last structures forming, with great implications for their cosmological use.

In fact, this kind of objects has become an important tool for Cosmology, in particular since they provide a way to estimate the total mass content in the Universe, to constrain cosmological parameters and to explore the process of structure formation that we will address in the following sections.

1.2 Composition of the Universe

Several observational features, such as rotation curves and velocity dispersion of galaxies, mass measurements of galaxy clusters or angular fluctuations in the spectrum of the CMB, suggested that the matter content of the Universe is mostly in a form invisible to us. The expression *Dark Matter* was created in order to stress this property of such unknown kind of matter. Moreover, the Universe seems to be formed for about the 73% by an unknown kind of energy, the so-called *Dark Energy*, that causes today an acceleration in its expansion. Thus, what we see is just about the 4% of the actual mass-energy content of the Universe, made of baryonic matter (usually including neutrinos) and radiation.

The origin of this composition is a very interesting theme in Cosmology.

The equations that govern the expansion of the Universe are derived by introducing a metric, which describes the space-time, and by using the formalism of General Relativity. Assuming homogeneity and isotropy, the most general space-time metric describing a universe in which the Cosmological Principle is obeyed is of the form of the Friedmann-Robertson-Walker (FRW) metric that can be written as:

$$ds^2 = -c^2 dt^2 + a(t)^2 \left[\frac{dr^2}{1 - kr^2} + r^2(d\theta^2 + \sin^2\theta d\phi^2) \right],$$

where t is the proper time, r , θ and ϕ are the spherical polar coordinates, and k is a parameter describing the curvature of the spatial hyper-surface and can take the values 0, corresponding to a flat space, 1, corresponding to a closed space, with finite volume and no boundary, and -1 , corresponding to an open, infinite space. $a(t)$ is called *scale factor* and it is related to the redshift by:

$$1 + z = \frac{a_0}{a},$$

where $a_0 \equiv a(t_0)$ is the scale factor at the present time.

We can also rewrite the Hubble constant in terms of this scale factor:

$$H_0 \equiv H(t_0) \equiv \frac{\dot{a}_0}{a_0},$$

which derives from the present time form of the more general Hubble parameter

$$H(t) = \frac{\dot{a}(t)}{a(t)}.$$

The observational value of the Hubble constant is $H_0 \simeq 70 \text{ km/s/Mpc}$ [52].

The General Relativity applied to the FRW metric yields two fundamental equations [10] called Friedmann equations:

$$\ddot{a} = -\frac{4}{3}\pi G \left(\rho + \frac{3p}{c^2} \right) a, \quad (1.1)$$

$$\dot{a}^2 + kc^2 = \frac{8}{3}\pi G \rho a^2, \quad (1.2)$$

where ρ and p are respectively the total energy density and the pressure of the Universe and the dot represents a derivative with respect to cosmological proper time t .

The density in the Universe is due to matter (baryonic and not baryonic) and radiation. In order to explain the present acceleration of the expansion of the Universe, a fluid for which gravity is repulsive has been introduced as one of the species in the present Universe (the mentioned dark energy). This new component is associated to a non-null cosmological constant Λ , whose density is:

$$\rho_\Lambda = \frac{\Lambda}{8\pi G}.$$

Hence, the total density can be written as the sum of all these components:

$$\rho = \rho_m + \rho_{rad} + \rho_\Lambda.$$

Conventionally, the abundance of each density component i is expressed by the dimensionless *density parameter*:

$$\Omega_i \equiv \frac{\rho_i}{\rho_c},$$

where

$$\rho_c \equiv \frac{3H^2}{8\pi G}$$

is called *critical density* and it is the energy density of a flat Universe ($k = 0$).

With this notation the three component parameters become:

$$\Omega_m = \frac{8\pi G \rho_m}{3H^2} \quad \Omega_{rad} = \frac{8\pi G \rho_{rad}}{3H^2} \quad \Omega_\Lambda = \frac{8\pi G \rho_\Lambda}{3H^2} = \frac{\Lambda}{3H^2},$$

so, when inserting these parameters in equation (1.2), we obtain the total density parameter as:

$$\Omega = \Omega_m + \Omega_{rad} + \Omega_\Lambda = \frac{8\pi G}{3H^2}(\rho_m + \rho_{rad} + \rho_\Lambda) = \frac{8\pi G}{3H^2}\rho = 1 + \frac{kc^2}{a^2H^2}$$

which describes the curvature of the Universe.

In fact:

$$\left\{ \begin{array}{ll} \text{if } \Omega > 1 & \rightarrow \rho > \rho_c \rightarrow k > 0 \text{ closed Universe} \\ \text{if } \Omega = 1 & \rightarrow \rho = \rho_c \rightarrow k = 0 \text{ flat Universe} \\ \text{if } \Omega < 1 & \rightarrow \rho < \rho_c \rightarrow k < 0 \text{ open Universe} \end{array} \right.$$

The values for the density parameters obtained from observational constraints are:

$$\left\{ \begin{array}{ll} \Omega_\Lambda & \simeq 0.73 \\ \Omega_{m, \text{DM}} & \simeq 0.23 \\ \Omega_{m, \text{bar}} & \simeq 0.04 \\ \Omega_{rad} & \simeq 10^{-5}, \end{array} \right.$$

with $\Omega_m = \Omega_{m, \text{DM}} + \Omega_{m, \text{bar}}$.

1.3 Structure Formation

The scenario of large scale structure formation is believed to begin from initial fluctuations in the density of any component of matter (dark matter, baryons) and radiation that arise in the very early Universe. Those fluctuations have grown through gravitational instability into the structures we observe today with a process that is thought to be hierarchical: the first perturbations to collapse are the smallest scale ones, and then the small scale objects merge and form larger structures through a continuous assembly mechanism.

The initial conditions depend on the adopted cosmological model of structure formation. The main elements involved are the background cosmology (a choice of the parameters Ω_m , H_0 and Ω_Λ), an initial fluctuation spectrum, a statistical distribution of fluctuations (often assumed to be Gaussian) and the proportion of particle species in the Universe (hot or cold dark matter, baryonic).

Since the Universe seems to be dominated by non-baryonic material, the dark matter component should drive the gravitational collapse and the hierarchical accretion of smaller systems. The first stage of the dark matter collapse is a sheet-like configuration, and subsequently the collapse continues toward elongated filaments, which eventually produce compact and virialized dark matter halos. The luminous matter follows the dark matter, so galaxies and galaxy clusters form at the centres of the dark matter haloes by cooling and condensation of baryons. This picture gives rise to the present observations of the cosmic web.

This process requires that the main component of dark matter is the so-called *cold dark matter* (CDM), made by particles that decouple while they are no longer relativistic. In this case the minimum value of the mass such that a perturbation can survive and grow is around $M \simeq 10^5 - 10^6 M_\odot$, since smaller fluctuations are destroyed by an effect called *free streaming*. This leads to the hierarchical scenario that is strongly supported by several observations.

1.4 Galaxy clusters

In this hierarchical scenario, galaxy clusters are the most recently formed systems in the Universe, held together by their own gravity. Their masses cover a range from roughly $10^{13} M_{\odot}$ to over $10^{15} M_{\odot}$, and their spatial size spreads over 1 – 3 Mpc. Dark matter represents $\sim 80\%$ of their total matter content while the most massive visible component is in diffuse, hot gas (15 – 20%), with stars and galaxies making up only for a few percent of the whole mass content of clusters (3 – 5%).

The large dark matter halos surrounding galaxy clusters as a first approximation can be described as spherical and isolated from their surroundings and their properties can be studied by performing high-resolution cosmological simulations. An important feature that emerges is that these systems seem to achieve a final state of equilibrium, displaying nearly universal density profiles. Julio Navarro, Carlos Frenk and Simon White (NFW) found that the density profiles of halos in CDM simulations can be fitted by the same formula, independently of their mass: ^[43]

$$\rho(r) = \frac{\rho_s}{\left(\frac{r}{r_s}\right) \left(1 + \frac{r}{r_s}\right)^2}.$$

This relation is parametrized by a characteristic length r_s , the scale radius, at which the logarithmic slope of the profile is $d \ln \rho / d \ln r = -2$, and the scale density $\rho_s = \rho(r_s)$. Within the scale radius, the DM density goes as $\rho \propto r^{-1}$, while beyond it the radial behavior is $\rho \propto r^{-3}$.

After the NFW work, several other functional forms have been proposed that can fit better the halos of higher resolution numerical simulation, both in the very inner and in the outer regions. The majority of these different results can be summarized in a compact universal form, the generalized NFW profile: ^[13]

$$\rho(r) = \frac{\rho_s}{\left(\frac{r}{r_s}\right)^{\alpha} \left(1 + \frac{r}{r_s}\right)^{\beta-\alpha}},$$

where the inner and the outer slopes, α and β , are not universal, but represent free parameters that can vary from halo to halo.

1.5 Clusters and Cosmology

As we discussed, clusters of galaxies occupy a special place in the hierarchy of cosmic structures. They arise from the collapse of initial perturbations having a typical comoving scale of about $10 h^{-1}\text{Mpc}$. According to the standard model of cosmic structure formation, the Universe is dominated by gravitational dynamics in the linear or weakly non-linear regime and on scales larger than this. In this case, the description of cosmic structure formation is relatively simple since gas dynamical effects are thought to play a minor role, while the dominating gravitational dynamics still preserves memory of initial conditions. On smaller scales, instead, the complex astrophysical processes, related to galaxy formation and evolution, become relevant. Gas cooling, star formation, feedback from supernovae (SN) and active galactic nuclei (AGN) significantly change the evolution of cosmic baryons and, therefore, the observational properties of the structures. Since clusters of galaxies mark the transition between these two regimes, they have been studied for decades both as cosmological tools and as astrophysical laboratories [7].

Constraints of cosmological parameters using galaxy clusters have been placed so far by applying different methods:

- the mass function of nearby galaxy clusters provides constraints on the amplitude of the power spectrum at the cluster scale. At the same time, its evolution provides constraints on the linear growth rate of density perturbations, which translates into dynamical constraints on the matter and dark energy density parameters; [46]
- the clustering properties (correlation function and power spectrum) of the large scale distribution of galaxy clusters provide direct information on the shape and amplitude of the underlying dark matter distribution power spectrum. Furthermore, the evolution of these clustering properties is again sensitive to the value of the density parameters through the linear growth rate of perturbations; [8] [42]
- the mass-to-light ratio (M/L) in the optical band can be used to estimate the matter density parameter, Ω_m , once the mean luminosity density of the Universe is known and under the assumption that mass traces light with the same efficiency both inside and outside clusters; [25]
- the baryon fraction in nearby clusters provides constraints on the matter density parameter, once the cosmic baryon density parameter

is known, under the assumption that clusters are fair containers of baryons ^[56]. Furthermore, the baryon fraction of distant clusters provides a geometrical constraint on the dark energy content and equation of state, under the additional assumption that the baryon fraction within clusters does not evolve. ^[18]

The mass function at redshift z , $n(M, z)$, is defined as the number density of virialized halos found at that redshift with mass in the range $[M, M + dM]$. The original derivation of the mass function expression was deduced by William H. Press and Paul Schechter ^[45] and is based on the assumption that the fraction of matter ending up in objects of a given mass M can be found by looking at the portion of the initial density field, smoothed on the mass-scale M , lying at an overdensity exceeding a given critical threshold value, δ_c . Under the assumption of Gaussian perturbations, the probability for the linearly-evolved smoothed field δ_M to exceed at redshift z the critical density contrast δ_c is:

$$p_{>\delta_c}(M, z) = \frac{1}{\sqrt{2\pi}\sigma_M(z)} \int_{\delta_c}^{\infty} \exp\left(-\frac{\delta_M^2}{2\sigma_M^2(z)}\right) d\delta_M.$$

From this expression, the number density can be obtained by:

$$\frac{dn(M, z)}{dM} = \frac{2}{V_M} \frac{\partial p_{>\delta_c}(M, z)}{\partial M} = \sqrt{\frac{2}{\pi}} \frac{\bar{\rho}}{M^2} \left| \frac{d \log \sigma_M(z)}{d \log M} \right| \exp\left(-\frac{\delta_c^2}{2\sigma_M^2(z)}\right),$$

where the factor 2 is a correction in order to recover the whole mass content of the Universe if we take the limit of arbitrarily small limiting mass.

In this expression, cosmological parameters enter through the mass variance σ_M , which depends on the power spectrum and on the cosmological density parameters, through $\bar{\rho} = \Omega_m \rho_c$, through the linear perturbation growth factor, and, to a lesser degree, through the critical density contrast δ_c . The mass function shape is dominated by the exponential tail so that it becomes exponentially sensitive to the choice of the cosmological parameters allowing to place tight constraints on them.

In order to pursue this analysis, we need a sample of galaxy clusters and a method to estimate their mass. We will widely discuss this last point in the next chapters. Concerning the identification of clusters, one of the most used way is through their X-ray emission. First of all, the X-ray selection has the advantage of revealing physically bound systems, because diffuse emission from a hot intracluster medium is the direct manifestation of the existence of a potential well within which the gas is in dynamical equilibrium with the cool baryonic matter (galaxies) and the dark matter.

Then, the X-ray luminosity is well correlated with the cluster mass and the X-ray emissivity is proportional to the square of the gas density, hence the cluster emission is more concentrated than the optical bidimensional galaxy distribution. In combination with the relatively low surface density of X-ray sources, this property makes clusters high contrast objects in the X-ray sky, and alleviates problems due to projection effects that affect optical selection. Another advantage of X-ray selection is the ability to define flux-limited samples with well understood selection functions. This leads to a simple evaluation of the survey volume and therefore to a straightforward computation of space densities. [7]

Fig. 1.3 shows an example of mass functions of clusters at low and high redshifts compared with predictions of a flat Λ CDM model and an open model without dark energy.

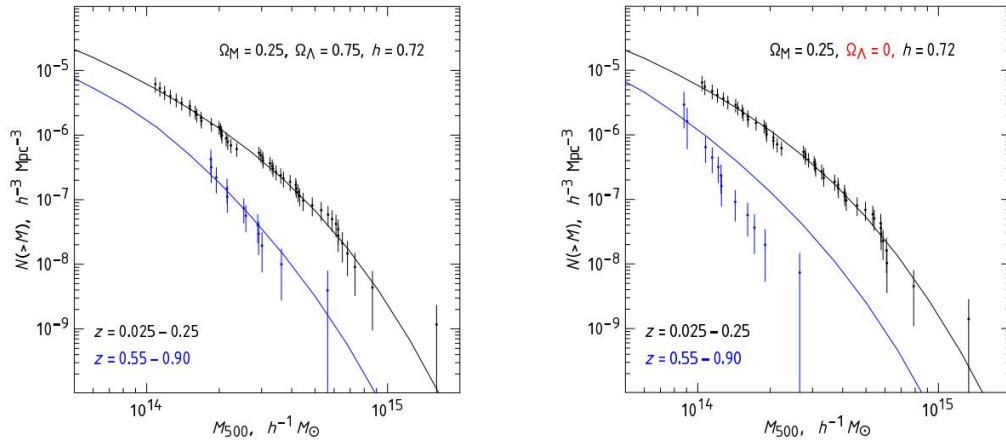


Figure 1.3: Measured mass functions of galaxy clusters at low (black) and high (blue) redshift compared with a flat model with Λ (left panel) and with an open model without Λ (right panel). [1]

Chapter 2

Mass estimation of galaxy clusters

As said before, galaxy clusters have become an important tool for Cosmology, in particular since they provide a way to estimate the total mass content in the Universe, to constrain cosmological parameters and to explore the process of structure formation.

The mass estimation of galaxy clusters is therefore a crucial point for modern Cosmology, and can be obtained by several different techniques, each one with its issues both theoretical and observational (first of all the impossibility of a direct observation of dark matter that is the main component of the matter content in a galaxy cluster).

Galaxy clusters are studied mainly in optical and X-ray bands, the first because of their content of galaxies and thus stars, the latter because of the diffuse hot gas that usually fills these structures. In addition, galaxy clusters are responsible of an effect predicted by Rashid Alievich Sunyaev and Yakov Borisovich Zel'dovich in 1969, that is a perturbation of the energy of the Cosmic Microwave Background photons when they undergo Inverse Compton scattering with high energy cluster electrons. This allows to study galaxy clusters also in microwaves and even to use these observations to find new galaxy clusters.

From these observable quantities it is possible to obtain a lot of information about the dynamics and the mass content of galaxy clusters.

2.1 Mass from virial theorem

The simplest way to compute the total mass of a galaxy cluster is by using the virial theorem, under the assumption of dealing with a virialized structure, i.e. a system of gravitationally interacting particles that is stable (in dynamical equilibrium). The scalar virial theorem can be expressed as follows:

$$2T + U = 0,$$

where T is the kinetic energy and U the potential energy of the system, that we can write for a uniform sphere of mass M and radius R ^[6] as:

$$T = \frac{1}{2} \sum_i m_i v_i^2 = \frac{1}{2} M \langle v^2 \rangle$$

$$U = -\frac{3}{5} \frac{GM^2}{R},$$

whence:

$$2 \cdot \frac{1}{2} M \langle v^2 \rangle = \frac{3}{5} \frac{GM^2}{R} \quad \longrightarrow \quad M \propto \frac{R \langle v^2 \rangle}{G}.$$

Under the assumption of spherical symmetry of the system and of a Gaussian velocity distribution, we can replace the mean squared velocity with the velocity dispersion:

$$\langle v^2 \rangle = 3\sigma_r^2$$

so:

$$M \propto \frac{R \sigma_r^2}{G}.$$

The radial velocity dispersion of a galaxy distribution is due to the different velocity that each galaxy in the cluster has, and can be obtained from the width of spectral lines of the cluster.

The first to apply this method was Fritz Zwicky in 1933 who came to the mass of the Coma cluster, observing only 8 galaxies ^[58].

2.2 Mass from Jeans equation

From the collisionless Boltzmann equation, that describes the time and space evolution of the distribution function of a system, we can obtain the spherical Jeans equation ^[5]:

$$\frac{d(\rho\sigma_r^2)}{dr} + 2\frac{\beta}{r}\rho\sigma_r^2 = -\rho(r)\frac{d\Phi}{dr}, \quad (2.1)$$

where $\rho(r)$ is the number density of the particles in the system, σ_r is the radial velocity dispersion, Φ is the gravitational potential and β is the anisotropy parameter defined by:

$$\beta \equiv 1 - \frac{\sigma_\theta^2 + \sigma_\phi^2}{2\sigma_r^2} \quad (2.2)$$

that quantifies the system's degree of radial anisotropy (σ_θ and σ_ϕ are the longitudinal and azimuthal velocity dispersions, equal if there is spherical symmetry).

Since we have

$$\frac{d\Phi}{dr} = \frac{GM(r)}{r^2}, \quad (2.3)$$

introducing equation (2.3) in (2.1) gives us:

$$\begin{aligned} M(r) &= -\frac{r^2}{\rho G} \left(\frac{d(\rho\sigma_r^2)}{dr} + 2\frac{\beta}{r}\rho\sigma_r^2 \right) \\ &= -\frac{r\sigma_r^2}{G} \left(\frac{r}{\rho\sigma_r^2} \frac{d(\rho\sigma_r^2)}{dr} + 2\beta \right) \\ &= -\frac{r\sigma_r^2}{G} \left(\frac{r}{\rho\sigma_r^2} \left(\frac{d\rho}{dr}\sigma_r^2 + \rho\frac{d\sigma_r^2}{dr} \right) + 2\beta \right) \\ &= -\frac{r\sigma_r^2}{G} \left(\frac{r}{\rho} \frac{d\rho}{dr} + \frac{r}{\sigma_r^2} \frac{d\sigma_r^2}{dr} + 2\beta \right) \\ &= -\frac{r\sigma_r^2}{G} \left(\frac{d \ln \rho}{d \ln r} + \frac{d \ln \sigma_r^2}{d \ln r} + 2\beta \right) \end{aligned}$$

where $M(r)$ is the mass responsible for the gravitational potential Φ , that is the total mass of the cluster (including gas and dark matter).

Even in this case the assumptions to make in order to obtain the expression for the mass and to assess the density profile and the radial velocity dispersion are sphericity and equilibrium of the system.

There is also an issue in the estimation of the anisotropy parameter, since β is allowed to be a free function of the radius, so a wide variety of mass profiles are consistent with given dispersion and density profiles ^[6]. So to the previous ones we have to add assumptions in order to characterize β .

2.3 Mass from hot gas emission

Galaxy clusters are immersed in a hot gas halo, at a temperature of $T \sim 10^7 - 10^8$ K. This gas emits by Bremsstrahlung in X-rays, providing a way to actually discover a cluster and, from the obtained spectrum, to compute its mass.

The assumption to do in this case is of hydrostatic equilibrium, that expresses the balance between the pressure tendency to expand the gas and the gravity tendency to collapse it:

$$\frac{dP}{dr} = -\frac{GM(r)}{r^2}\rho.$$

Moreover, for an ideal gas the state equation is

$$P = \frac{\rho}{\mu m_H}kT$$

so:

$$\frac{dP}{dr} = \frac{k}{\mu m_H} \left(T \frac{d\rho}{dr} + \rho \frac{dT}{dr} \right).$$

Combining these two equations we can obtain:

$$\begin{aligned} M(r) &= -\frac{k}{\mu m_H G} \left(T \frac{d\rho}{dr} + \rho \frac{dT}{dr} \right) \frac{r^2}{\rho} \\ &= -\frac{kT}{\mu m_H G} \left(\frac{r}{\rho} \frac{d\rho}{dr} + \frac{r}{T} \frac{dT}{dr} \right) r \\ &= -\frac{kT}{\mu m_H G} \left(\frac{d \ln \rho}{d \ln r} + \frac{d \ln T}{d \ln r} \right) r. \end{aligned}$$

We can see how the dependence on the gas temperature is much stronger than that on the gas density.

Anyhow we need to know $T(r)$ and $\rho(r)$, that can be derived from X-ray imaging data. The X-ray emission ε_X in each point in the cluster is in fact sensitive to the number density n in that point. So azimuthally averaging the X-ray emission it is possible to obtain the density profile of the gas.

In fact we have:

$$\Sigma_X(b) = \int \varepsilon_X dl = \int_b^\infty n_e n_i \Lambda(T) \frac{2r dr}{\sqrt{r^2 - b^2}},$$

where b is the projected radius and $\Lambda(T)$ is the cooling function.

This can be “Abel inverted” to obtain:

$$\varepsilon_X = -\frac{1}{2\pi r} \frac{d}{dr} \int_{r^2}^\infty \frac{\Sigma_X(b) db^2}{\sqrt{b^2 - r^2}}.$$

Since the emissivity is given by $\varepsilon_X \propto n_e^2 \Lambda(t)$, knowing it we can come to the density profile ^[17].

In Fig. 2.1 is shown the X-ray surface brightness for the galaxy cluster Abell 2319 (Cygnus) whence we can find the density n .

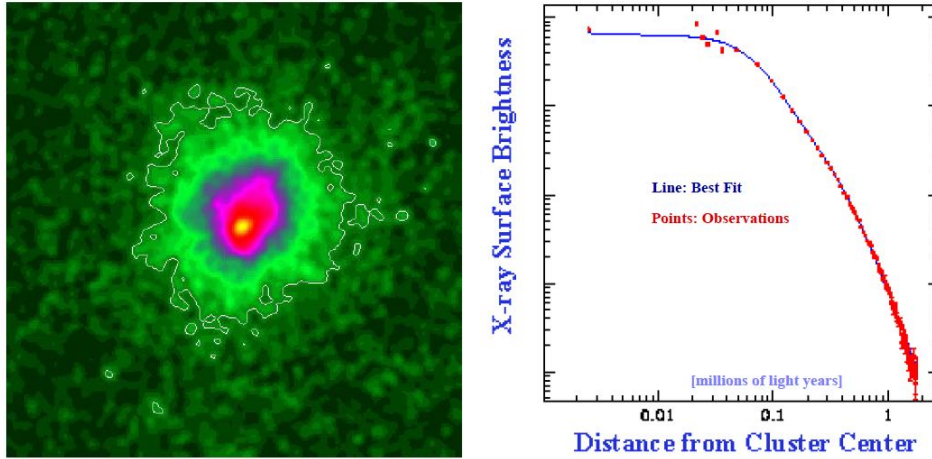


Figure 2.1: (*Left panel*): Roentgen Satellite X-ray Image of Galaxy Cluster Abell 2319. (*Right panel*): X-ray surface brightness as a function of the distance from the cluster center (red points) with a so-called β -model to fit the data (blue line). ^[12]

So the steps to arrive to the density profile are:

- choosing a center for the cluster;
- azimuthally averaging the X-ray emission (right panel of Fig. 2.1);
- fitting this emission to model the X-ray profile;
- calculating the implied density profile.

Then, to know $T(r)$, it is necessary taking spectra from different locations in the cluster (typically along rings around the cluster center) and looking at the shapes of these spectra, as shown in Fig. 2.2.

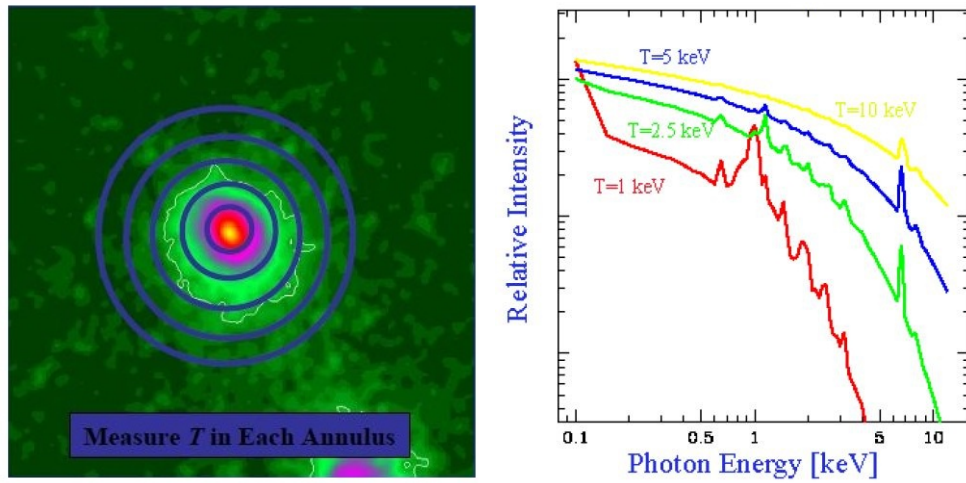


Figure 2.2: Rings around the center of the cluster (*left*) and corresponding possible spectra (*right*) to infer the temperature profile. ^[12]

The spectral features, like lines and cut-off, are in fact sensitive to T . If we have a gas with $T \sim 10^7$ K the Fe-L lines are particularly important (red spectrum). Instead, for a gas at $T \sim 10^8$ K the continuum shape and the Fe- $K\alpha$ line become more relevant (yellow spectrum). Even for this method the main complication is its relying on the assumption of spherical symmetry.

2.4 Mass from gravitational lensing

According to the weak equivalence principle from General Relativity theory, if we look at the free fall motion of a body inside an enclosed room it's not possible to discern whether that body is under the influence of a gravitational field or of an inertial force. This leads to the fact that a gravitational potential is able to bend light.

Orest Chowlos and Albert Einstein predicted that if a background object is directly aligned with a point source mass, the light rays will be deflected into a ring (the so-called *Einstein Ring*). Then, Zwicky predicted that it could be possible to study the mass distribution in clusters by studying background galaxies that are lensed by the matter in the cluster. This wasn't observationally feasible until the mid-90's, but it is now a well known method to derive the mass of galaxy clusters.

Consider a photon moving past a point mass M . From classical Newtonian Gravity the photon will undergo an acceleration perpendicular to the direction of its motion:

$$\frac{dv_{\perp}}{dt} = \frac{GM}{r^2} \sin \theta.$$

Integrating along the path we can find the deflection of the photon (Fig. 2.3):

$$v_{\perp} = \frac{GM}{c} \int_{-\infty}^{\infty} \frac{1}{x^2 + \xi^2} \frac{\xi}{(x^2 + \xi^2)^{1/2}} dx = \frac{GM}{c} \xi \int_{-\infty}^{\infty} (x^2 + \xi^2)^{-3/2} dx,$$

where $dx = cdt$. The solution is:

$$v_{\perp} = \frac{2GM}{\xi c}$$

so the deflection angle is:

$$\alpha_{Newt} = \frac{v_{\perp}}{c} = \frac{2GM}{\xi c^2}.$$

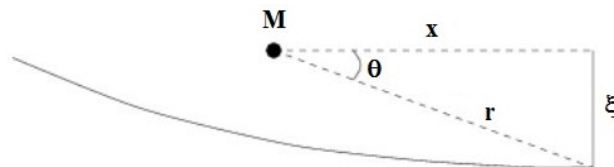


Figure 2.3: Deflection in the path of a photon created by a point mass M .

In General Relativity, gravity influences also the time component of the photon's path, so the deflection angle becomes:

$$\alpha_{GR} = \frac{4GM}{\xi c^2}.$$

From the law of sines on the triangle OSI (see Fig. 2.4):

$$\frac{\sin(180^\circ - \alpha)}{D_s} = \frac{\sin(\theta - \beta)}{D_{ds}}$$

and since β , θ and α are very small, we can use the small angle approximation $\sin(\theta - \beta) \sim \theta - \beta$ and $\sin(180^\circ - \alpha) = \sin \alpha \sim \alpha$, whence:

$$\beta = \theta - \frac{D_{ds}}{D_s} \alpha.$$

Whereas $\theta \sim \sin \theta = \xi/D_d$ and we know α , we have:

$$\beta = \theta - \left(\frac{4GM}{c^2} \frac{D_{ds}}{D_d D_s} \right) \frac{1}{\theta}.$$

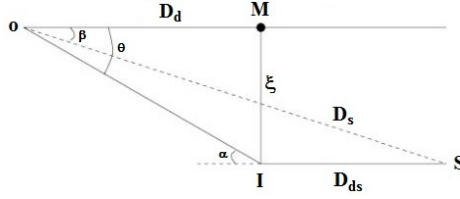


Figure 2.4: Schematic view of the image I of a source S seen by an observer O if the photons of the source pass nearby a point mass M .

When $\beta = 0$ the source S is directly behind the lens M , so we have the Einstein Ring at an angle ^[22]

$$\theta_E = \sqrt{\frac{4GM}{c^2}} \sqrt{\frac{D_{ds}}{D_d D_s}}$$

and we can define a critical surface density ^[22] such that lensing occurs:

$$\Sigma_{crit} \equiv \frac{c^2}{4\pi G} \frac{D_s}{D_d D_{ds}} \frac{1}{(1+z_L)^2},$$

so that we have lensing if:

$$\frac{M(< \xi_E)}{\pi \xi^2} > \Sigma_{crit}.$$

The resulting source image is characterized by two quantities, the shear, that quantifies the gravitational field of the lensing mass distribution and is responsible for the image distortion, and the convergence, that causes the image contraction.

The convergence k is related to the surface mass density Σ of the lens by ^[2]:

$$k \equiv \frac{\Sigma}{\Sigma_{crit}},$$

while the shear has two components, related to the potential by ^[2]:

$$\begin{cases} \gamma_1 = \frac{1}{2} \left(\frac{\partial^2 \Phi}{\partial x_1^2} - \frac{\partial^2 \Phi}{\partial x_2^2} \right) \\ \gamma_2 = \frac{\partial^2 \Phi}{\partial x_1 \partial x_2}. \end{cases}$$

A measure of the convergence and the shear allows to recover the lens potential, and so the cluster mass.

There are two kinds of lensing that can be observed with a cluster, the so called strong and weak lensing.

When $\Sigma > \Sigma_{crit}$ the presence of a distant source, such as a galaxy, produces elongated curves, called giant arcs. The strong lensing is usually characterized by the production of multiple images from a single source. In this case of the strong lensing, the location of an arc provides a measure of the cluster mass within the circle traced by the long arc. Since it requires a high density of the lens, the strong lensing is suited for the study of the cluster density profiles in the inner regions ($< 0.1 h^{-1}$ Mpc).

In addition to the giant arcs, a cluster can also produce weakly distorted images of a large number of background galaxies. These images are called arclets. The weak lensing is instead caused by any density fluctuation, and therefore it can be used for the determination of the mass profile also in the outer regions of galaxy clusters. However, the weak signal from individual arclets needs to be statistically averaged over several sources. This feature limits the precision with which masses are determined.

The weak lensing methods suffer from the important problem of the mass sheet degeneracy. This means that the projected mass profile can be determined only up to a degeneracy addition of an arbitrary constant, due to the projection effects. Assumptions on the mass distribution are needed in order to constrain the constant value. The advantage of these methods is that, in contrast to other dynamical techniques for probing gravitational fields, no assumption needs to be made on the dynamical state of the matter.

If we have an extended source, such as a cluster, the geometry becomes much more complex but it can still be modeled so that we can find the mass distribution of the cluster. The arcs are formed near the critical curve $\theta = \theta_E$ (with small β) and from the radius of these arcs we can derive the enclosed mass [22].

Gravitational lensing preserves surface brightness, but changes the solid angle subtended by a source. Thus, the total flux is magnified so this method can be used to find sources that without lensing would be too faint to be seen. The magnification is given by the ratio of the areas of the source and of the lensed image:

$$\mu = \frac{\theta d\theta}{\beta d\beta}.$$

However, the weakness of the lensing method is its high sensitivity to the resolution of the instrument and to projection effects.

In Fig. 2.5 there is a representation of the way we see a source whose light is perturbed by the gravitational potential of a galaxy cluster, depending on the angle of the line of sight, while in Fig. 2.6 there are images of Abell 2218 and SDSS J1050+0017 that clearly show lensing arcs.

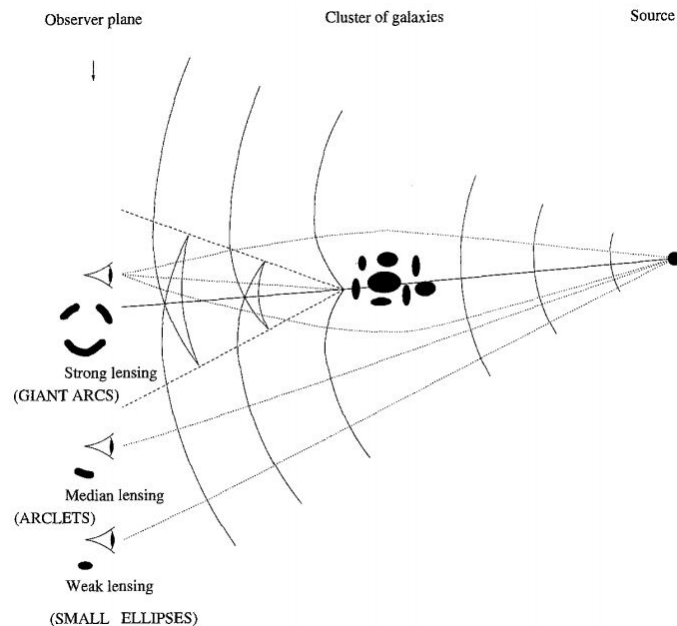


Figure 2.5: Schematic view of the perturbed wavefronts. [22]

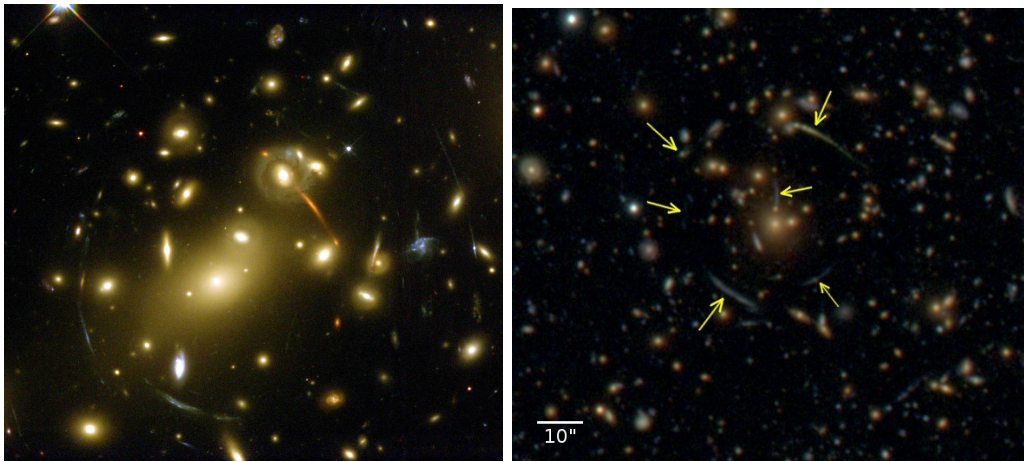


Figure 2.6: Lensing arcs in Abell 2218 (*left*) [image from NASA/ESA] and SDSS J1050+0017 (*right*) [image from Subaru/Suprime-cam].

2.5 Mass from Sunyaev-Zel'dovich effect

As told before, the intracluster medium is gas at a temperature $k_B T_e$ from 5 to 15 keV, rarefied, with peak electron number density $n_e \simeq 10^{-3} \text{cm}^{-3}$, that cools mainly via thermal Bremsstrahlung in the X-ray band. We observe a distortion of the Cosmic Microwave Background radiation, due to Inverse Compton scattering of the cool photons of the CMB off these hot Intra Cluster Medium (ICM) electrons, called Sunyaev-Zel'dovich effect (SZE) [53].

At frequencies smaller than ~ 218 GHz the intensity of the CMB is reduced because the photons are scattered at higher energies, so the SZE is manifested as a brightness temperature decrement towards the cluster, with a correspondent increment for frequencies above 218 GHz, where the photons are scattered. This variation is proportional to the Compton parameter:

$$\frac{\Delta T_{SZE}}{T_{CMB}} = f(x)y,$$

where

$$y \equiv \frac{k_B \sigma_T}{m_e c^2} \int n_e(l) T_e(l) dl$$

is the Compton parameter, which for an isothermal cluster equals the optical depth τ_e times the fractional energy gain per scattering. σ_T is the Thomson cross-section, n_e is the electron number density, T_e is the electron temperature, k_B is the Boltzmann constant, $m_e c^2$ is the electron rest mass energy, and the integration is along the line of sight.

In Fig. 2.7 is shown a representation of the distortion in CMB spectrum caused by a galaxy cluster.

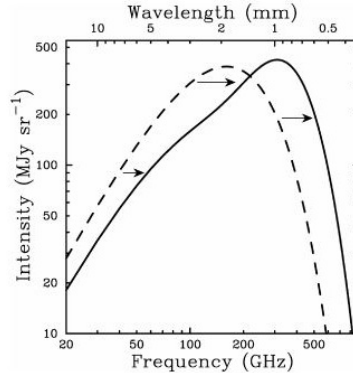


Figure 2.7: SZE spectral distortion of the CMB spectrum for a fictional cluster 1000 times more massive than a typical massive galaxy cluster. [9]

A very important feature of this effect is that $\Delta T_{SZE}/T_{CMB}$ is independent of redshift, so this makes the SZE a potentially powerful tool for investigating the high-redshift Universe [9].

From observations of the SZE, once the electron temperature is known (from the SZE itself [28] or for example from X-ray emission), it is possible to directly measure the gas mass in the cluster. The total gravitating mass can be determined by assuming hydrostatic equilibrium and modeling the distribution of the gas and the electron temperature. Using a spherical isothermal β -model for the ICM, the resulting total mass of the cluster within radius r is:

$$M(r) = \frac{3kT_e\beta}{G\mu m_p} \frac{r^3}{r_c^2 + r^2},$$

where μm_p is the mean molecular weight of the gas, usually calculated assuming solar metallicity for the gas and that μ is constant throughout the gas. r_c (the core radius) and β are fit parameters that enter in the electron number density [27].

The cluster gas mass fraction can also be measured by comparing SZE-derived gas masses and weak lensing-derived total masses. In this way gas mass fraction can be derived without assuming neither a model for the cluster structure nor hydrostatic equilibrium, so that there is no need to parametrize the ICM distribution.

Moreover, the gas mass fraction is believed to be a reasonable estimate of the baryonic mass fraction of the cluster, which should also be a good approximation of the universal baryonic mass fraction:

$$f_B \equiv \frac{\Omega_B}{\Omega_M}.$$

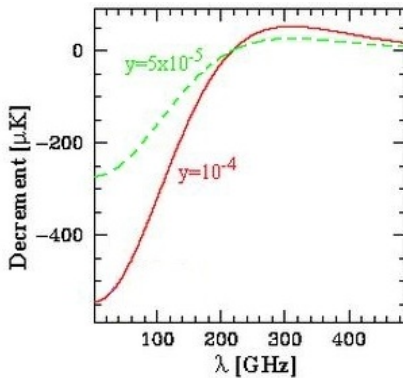


Figure 2.8: Strength of the SZ effect for two clusters with different total masses (dashed lower than solid). On the vertical axis there is the difference between the Cosmic Microwave Background signal and the SZ signal. This clearly shows that the SZ effect depends directly on the total cluster mass. [9]

2.6 Mass from caustic technique

Looking at the outskirts of galaxy clusters, where the usual assumption of dynamical equilibrium is not valid, it is possible to develop a mass estimator that relies on kinematic data only ^[16].

In fact the sphere of influence of a cluster extends well beyond the virial radius drawing the galaxies around the clusters to detach from the overall Hubble expansion of the Universe and slowly fall towards the cluster, forming a coherent infall pattern extending out to 10 – 20 Mpc from the cluster. As they fall inwards they are accelerated by the gravitational potential of the cluster, reaching a maximal velocity as they pass through the cluster for the first time. They then ultimately become virialized members, orbiting on bound orbits around the cluster. This behavior produces the characteristic “trumpet”-shaped caustic profile of galaxies infalling and orbiting around a massive cluster when we look them in the redshift space.

This caustic profile allows the identification of all those galaxies within the sphere of influence of the cluster (including the ones beyond the virial radius) as those lying within the caustic itself.

The width of the caustic profile is a function of cluster-centric radius and can be used to measure the mass profile of the cluster, not just within the virial radius, but beyond. The width of the profile at a given radius can be associated to the escape velocity a galaxy would have at that distance from the cluster.

Half of the redshift space distance between the upper and the lower caustic at projected separation r from the cluster center defines the amplitude $\mathcal{A}(r)$. Assuming spherical symmetry, $\mathcal{A}(r)$ is a measure of the gravitational potential $\Phi(r)$.

The escape velocities of galaxies are in fact deeply connected to the gravitational potential of the cluster, as we can see by:

$$v_e^2(r) = -2\Phi(r).$$

From the estimation of the caustic amplitude from the phase space, we can therefore arrive to relate it to the gravitational potential, and thus the mass, of the cluster:

$$GM(< r) = \int_0^r \mathcal{A}^2(R) \mathcal{F}_\beta(R) dR,$$

where \mathcal{F}_β is related to the anisotropy profile β and to the potential Φ by ^[16]:

$$\mathcal{F}_\beta(r) = -2\pi G \frac{\rho(r) r^2}{\Phi(r)} \frac{3 - 2\beta(r)}{1 - \beta(r)}.$$

β is the velocity anisotropy parameter defined by eq. (2.2).

In a hierarchical clustering scenario \mathcal{F}_β is a slowly changing function of r and so can be assumed constant. Moreover the value of 1/2 provides accurate mass profiles in N-body simulations and also in real clusters, when compared with masses obtained with other methods.

In this way the mass resulting from the caustic method can be written in a very simple way:

$$GM(< r) = \frac{1}{2} \int_0^r \mathcal{A}^2(R) dR.$$

So the advantage of this method is that it only requires the galaxy positions and velocities in and around the cluster.

In Fig. 2.9 there is an example of the diagrams used in the caustic method.

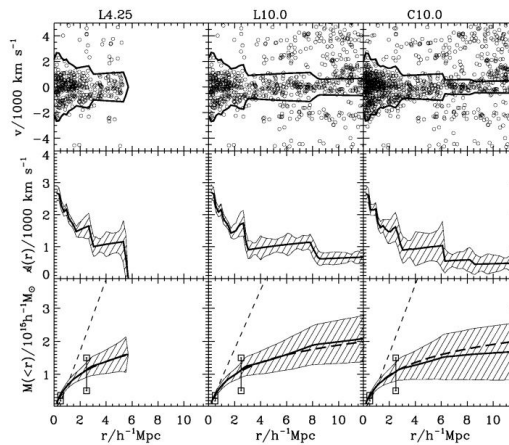


Figure 2.9: (*Top panels*) Galaxy distribution in the redshift diagram of Coma for three galaxy samples of increasing size. The bold lines indicate the location of the caustics. (*Middle panels*) Half of the distance between the caustics, that defines the amplitude $\mathcal{A}(r)$. (*Bottom panels*) The bold lines are the caustic mass profiles. The two error bars show the range of the X-ray mass estimates. Short-dashed and long-dashed lines are the cumulative mass profile for a softened isothermal sphere and a NFW density profile. Shaded areas in the middle and bottom panels indicate the 2σ uncertainty. [24]

The correct determination of the caustic curve is a crucial point for the accuracy of this method, so it is necessary to be very careful in the definition of the cluster borders and in the identification of the infalling galaxies in the phase space.

A precise caustic surface amplitude is achieved when a large number of

galaxy members, in and outside clusters, is available. So the method could be affected by uncertainties when applied to poorly populated clusters. Moreover, a crucial role is played by the selection of members and the interlopers removal. Thus, the main uncertainty is introduced by projection effects.

Another issue resides in the approximation of \mathcal{F}_β with a constant. Although it is very useful to make the analysis independent of the anisotropy profile, the parametrization of \mathcal{F}_β , and so $\beta(r)$, with a function which changes with r might improve the results on the clusters mass estimation.

However, the caustic method relies only on assumptions about the shape of the cluster, not about its dynamical state. Svensmark et al. (2014) ^[54] perform an interesting analysis about the validity of these assumptions. They demonstrate the effect of spatial anisotropy of galaxy clusters on the inferred caustic mass profiles of N-body simulated samples. They find that a line of sight along the major axis overestimates the caustic mass of galaxy clusters, as well as a line of sight along the minor axis underestimates it, and this discrepancy between major and minor axis mass estimates can arrive to a factor of ~ 2 within the virial radius, an up to ~ 3 within $3R_v$. So, the caustic method of mass estimation performs well when the condition of cluster sphericity is met. If however some spatial anisotropy is present in the form of cluster elongation of filamentary structures, the caustic masses are strongly dependent on the line of sight through the cluster, even within the virial radius.

We will come back on this point in the last chapter of this work.

Chapter 3

A new method to measure the mass of galaxy clusters

As we saw in the previous chapter, every method to estimate the mass of galaxy clusters relies on strong assumptions about the dynamical or hydrodynamical conditions of the cluster, or about its geometry.

In order to develop a way to estimate the mass of a cluster which is detached from all these assumptions, it's necessary to find a tool which is independent of a model for shape, state or content of the structure but only relies on the actual gravitational potential, and so the total mass, of the cluster.

Falco et al. (2014) ^[20] proposed a completely new method that infers the total cluster mass from the knowledge of the kinematics of the outskirts, where the matter has not yet reached equilibrium. They analyze the filamentary and sheet-like structures outside the cluster and see how the gravitational potential of the cluster perturbs their Hubble motion with the expanding Universe.

They characterize the radial velocity profile of these structures and use it to estimate not only the virial mass of the cluster, but also the three-dimensional orientation of the structures they find, providing an interesting method to explore the properties of the cluster even in the three-dimensional space.

The purpose of this thesis is to improve the method they developed, particularly in the way of finding these structures, and then to try to use it to explore the three-dimensional orientation and shape of simulated haloes and real clusters.

3.1 Radial infall velocity profile

There is a region where the matter in the cluster is approximately in dynamical equilibrium. The radius of this virialized region r_v is the distance from the center of the cluster within which the mean density is Δ times the critical density of the Universe ρ_c :

$$\rho(r_v) = \Delta\rho_c,$$

so the virial mass is given by

$$M_v = \frac{4}{3}\pi r_v^3 \Delta\rho_c$$

with

$$\rho_c = \frac{3H^2}{8\pi G},$$

where H is the Hubble constant and G the universal gravitational constant. The circular velocity at $r = r_v$ is defined as:

$$V_v^2 \equiv \frac{GM_v}{r_v}$$

and is called virial velocity.

Galaxy clusters are surrounded by galaxies and groups of galaxies outside the virial radius, which are not part of the virialized cluster but are still gravitationally bound to it, so that they fall towards the cluster center. This region in which the infall motion is predominant extends up to three or four times the virial radius, while beyond six to ten r_v the radial motion of galaxies is dominated by the Hubble flow.

In between, the cluster still expresses its gravitational influence, perturbing the flowing of the galaxies away from it, and leading to a deceleration of these structures.

So the total mean radial velocity of galaxies outside the cluster is given by these two effects:

$$\bar{v}_r(r) = Hr + \bar{v}_p(r),$$

where the term Hr represents the pure Hubble flow and $\bar{v}_p(r)$ is a mean negative infall term that takes into account the perturbation from the Hubble relation.

The more massive the cluster is, the stronger will the perturbation be, so we can explicitly write this dependence inside the equation:

$$\bar{v}_r(r, M_v) = Hr + \bar{v}_p(r, M_v). \quad (3.1)$$

Thus, we need to find the relation between $\bar{v}_p(r, M_v)$ and M_v in order to infer the virial mass of the cluster from the perturbed motion of the structures outside.

From simulated halos we saw a quite universal trend for the radial mean velocity profile when normalized to the virial velocity and to the virial radius. This can be seen in Fig. 3.1 which shows the profiles of three simulated halos and the simultaneous fit to them.

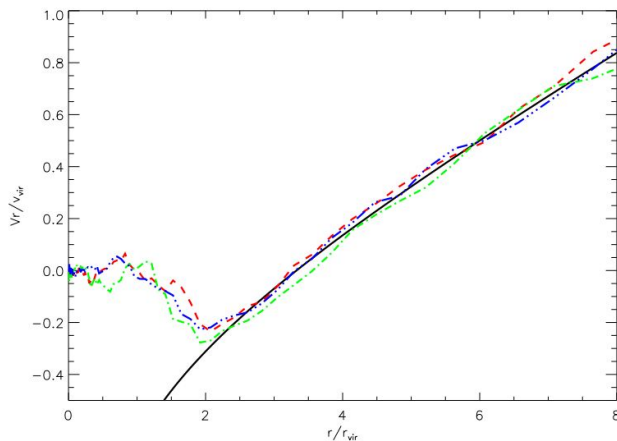


Figure 3.1: Mean radial velocity profiles for three simulated halos (dashed lines) and simultaneous fit to them (solid line). The virial masses of these halos are: $M_v = 0.8 \cdot 10^{14} M_\odot$ (blue triple-dot dashed line), $M_v = 1.1 \cdot 10^{14} M_\odot$ (green dot dashed line), $M_v = 4.7 \cdot 10^{14} M_\odot$ (red dashed line). ^[20]

It is now necessary to parametrize this infall profile. We use just the information that it must reach zero at large distances from the halo, so, in the region where the Hubble flow starts to dominate and the total mean radial velocity becomes positive, the infall term is given with good approximation by:

$$\bar{v}_p(r) \approx -v_0 \left(\frac{r}{r_v} \right)^{-b} \approx -aV_v \left(\frac{r}{r_v} \right)^{-b}. \quad (3.2)$$

Fitting the universal shape of the simulated halos profile with this equation, and taking a and b as free parameters, the result is the black solid line in Fig. 3.1, corresponding to the following value of the parameters:

$$\begin{cases} a = 0.80 \\ b = 0.42. \end{cases}$$

We now need to obtain a two-dimensional projected equation from the three-dimensional radial equation (3.2), since the observations give us a two-dimensional map of clusters and their surroundings through the component of the galaxies velocity along line of sight v_{los} and their projected distance on the sky R .

Consider the galaxies belonging to a filamentary structure outside the cluster: if we call α the angle between their 3D radial position (r) and the 2D projected distance (R), the relations between quantities in the physical space and in the so-called redshift space are:

$$\begin{cases} R = r \cos(\alpha) \\ v_{los}(R) = v_r(r) \sin(\alpha). \end{cases}$$

Inserting equation (3.1) in the transformation of the velocity we obtain:

$$v_{los}(R, \alpha, M_v) = \sin(\alpha) \left[H \frac{R}{\cos(\alpha)} + v_p \left(\frac{R}{\cos(\alpha)}, M_v \right) \right].$$

Using the model discussed before for the infall term that is equation (3.2), the line of sight velocity becomes:

$$v_{los}(R, \alpha, M_v) = \sin(\alpha) \left[H \frac{R}{\cos(\alpha)} - aV_v \left(\frac{R}{\cos(\alpha) r_v} \right)^{-b} \right]. \quad (3.3)$$

Using this equation it's possible to obtain the cluster virial mass M_v and the orientation angle of the structure α just knowing the phase-space coordinates (R, v_{los}) of the galaxies in a filament or sheet, with (M_v, α) as free parameters.

3.2 Identification of filaments and sheets

An observation of a galaxy cluster with its outskirts gives us the positions and velocities of the galaxies projected on the sky, that is: x, y, v_z .

From this information we need to find structures that have a filamentary or sheet-like shape in this (x, y) plane.

Indeed we are looking for an overdensity of galaxies, so we need to compare our part of the sky with a background; to do this, we split the spatial distribution of galaxies into eight two-dimensional wedges, and we look at each of them in the (R, v_{los}) space where we look for overdensities.

3.2.1 Cells

For each wedge the purpose is to compare the galaxy number density with the same quantity averaged on the rest of the wedges. To this aim, Falco et al. (2014) confine the velocity field to the box $v_{los} = [-4000, 4000]$ km/s and $R = [4, 20]$ Mpc, and divide this box into 50 cells, 4 Mpc large and 400 km/s high. We can see an example of one of these wedges both in the (x, y) plane and in the (R, v_{los}) plane in Figs. 3.2 and 3.3.

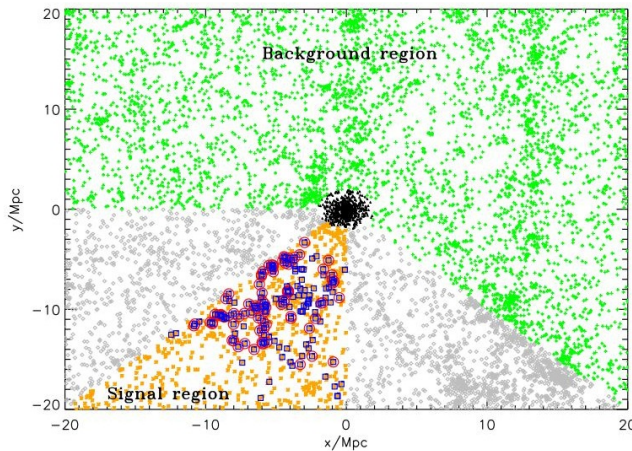


Figure 3.2: 2D projection of the simulation box, centered on the selected simulated halo. The black triangles represent the particles inside the virial radius of the halo. The orange points belong to one of the eight wedges they select in the (x, y) plane. The background for the selected wedge is given by the green crosses. The two wedges adjacent to the selected wedge, gray diamonds, are excluded from the analysis. In the selected wedge, they identify a sheet that is represented by the red circles. The blue squares correspond to the total overdensity found in the wedge. ^[20]

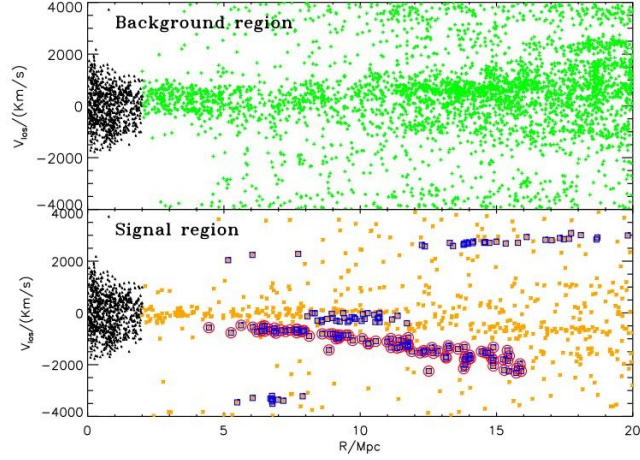


Figure 3.3: Line of sight velocity v_{los} as function of the projected distance R from the center of the simulated halo. (*Upper panel*) Background region (green crosses) obtained from the superposition of all the wedges but the selected one and the two adjacent ones (gray diamonds). (*Bottom panel*) Signal region (orange points) i.e. the selected wedge. The blue points correspond to the overdensity in the wedge while the red circles represent the filamentary-like structure they identify as a sheet, that is the only almost straight inclined line. The black triangles are all the particles within the virial radius of the halo. ^[20]

Then they count the number density of galaxies n_i in each cell i , and compare it to the same quantity computed for the rest of the wedges in the same cell. This is actually the average of the galaxy number density over all the wedges but the selected one. This quantity acts as the background n_i^{bg} . The two wedges adjacent to the selected one are excluded from the background since a possible structure sitting in the selected wedge might stretch even to the closest wedges.

Given these two quantities, they evaluate the overdensity as:

$$m_i = \frac{n_i - n_i^{bg}}{n_i^{bg}} \quad (3.4)$$

and then they calculate the probability density $p(m_i)$ for the given wedge. They use this probability density to decide if keeping the value of m_i found as an overdensity or not. They in fact take only the cells in the top 1σ region of the probability density distribution where the integrated probability is above $(100 - 16.8)\%$ in order to reduce the background noise.

There is another criterion they use to choose the structures: among the galaxies belonging to the selected cells, they take just the ones lying on inclined lines within a small scatter, while they remove the groups which appear as blobs or horizontal strips in the phase-space. This because their (and our) only interest is in extended structures with a coherent flow relatively to the cluster.

3.2.2 Rectangles

As we said before, we are interested in finding filamentary and sheet-like structures. So we can develop a more sophisticated method to identify them in the redshift space. Instead of splitting the phase-space in small cells, looking for overdensities in each cell, and selecting the overdense regions that form the elongated structure, we identify the overdensities taking into account the fact that we need long quasi-linear structures.

So we build a rectangle around each galaxy in the (R, v_{los}) plane, and we vary width, length and orientation of this rectangle by generating random numbers. For each of these rectangles, we evaluate the overdensity by comparing the number galaxy density in the rectangle to the same number in the background region, using the same relation as before:

$$m_i = \frac{n_i - n_i^{bg}}{n_i^{bg}}, \quad (3.4)$$

thus, we look for the rectangle which maximizes m_i .

Fig. 3.4 shows an example of possible rectangles built around a galaxy. It is evident that they contain a different number of galaxies, even though this number has to be compared with the background.

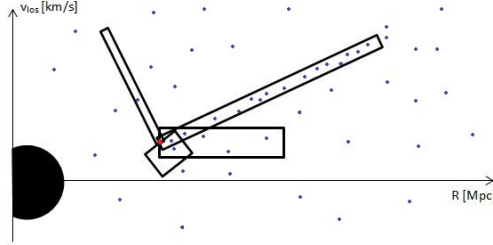


Figure 3.4: Schematic view of a galaxy outside a cluster and possible rectangles with variable width, length and orientation.

So, for each galaxy in the wedge we are considering, we have a maximized value of m_i and a rectangle that identifies a filamentary structure in the phase-space. Now we need a method to discern between all these rectangles (from all the different galaxies), because not all of them correspond to an actual overdensity. We use several criteria to do this. First of all we consider just the overdensities above 3σ in the distribution $N(m_i)$. In this way we select only the overdensities above a given threshold, likewise Falco et al. (2014) do with the grid method.

As example we show this distribution for one of the simulated halos we will analyze in the next chapter, so that we can see the histogram with the overdensities (Fig. 3.5).

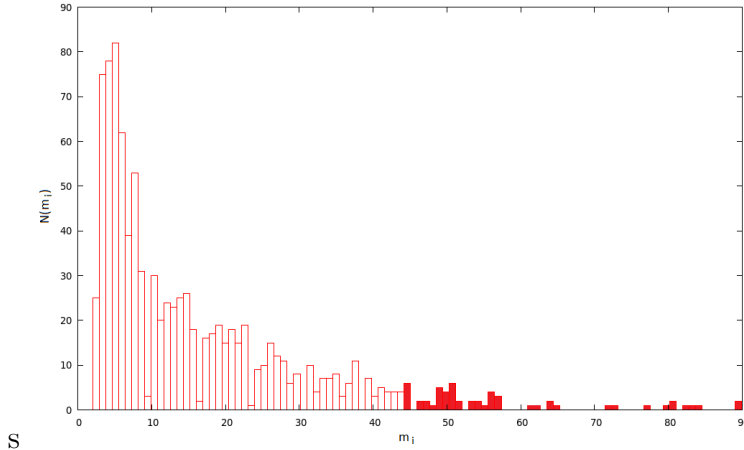


Figure 3.5: Distribution of the overdensities for a simulated halo. The full-colored bins are the ones above 3σ of the distribution, which we keep in our analysis.

Then, we can use the fact that if we have an overdensity, the rectangles corresponding to the galaxies belonging to this overdensity should overlap and have similar orientations. So we look at the distribution of these angles, and we search for the peaks in this distribution. These peaks represents the fact that a lot of rectangles have the same angle, and thus they show the orientation of the overdensities. We select just the rectangles with an angle that has a peak above 3σ the average value of the distribution. The 3 bins around the angle $\theta = 0$ are removed, since they correspond to horizontal structures that we want to exclude. Fig. 3.6 shows this selection for the same halo of the previous histogram.

The last information we use, is the fact that we are looking for structures with a coherent motion toward the cluster. So the galaxies in these structures should lie on inclined lines in the (R, v_{los}) space, and thus if we extend the rectangles corresponding to these galaxies they should cross the line $v_{los} = 0$ somewhere quite close to the cluster center. So, we select the rectangles with a crossing point between 0 and 8 Mpc, in order to exclude all these horizontal structures. Fig. 3.7 clarifies this property.

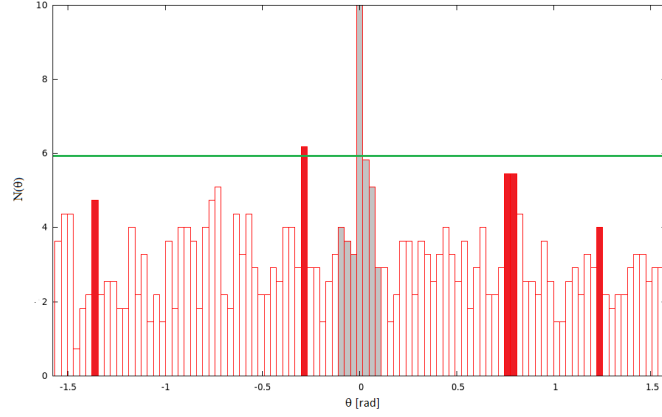


Figure 3.6: Distribution of the orientation angles of the rectangles in a wedge. The gray central bins are the removed ones. The green horizontal line corresponds to the value $\langle N(\theta) \rangle + 3\sigma_{N(\theta)}$ and the red bins are the same of Fig. 3.5. Only one of them is above the threshold line, so it represents the orientation of the structure we are looking for.

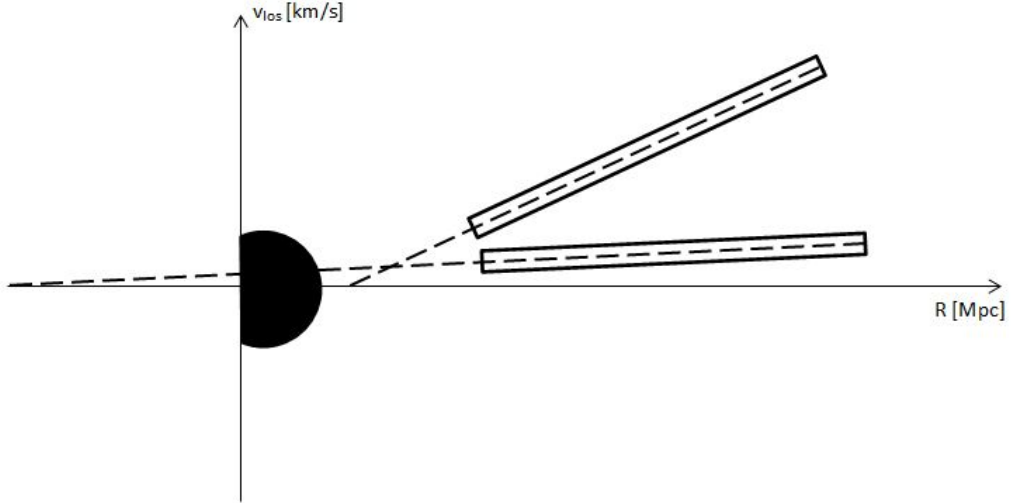


Figure 3.7: Crossing point for two rectangles with different inclinations. The rectangle almost flat crosses the line $v_{los} = 0$ in a point with a negative value of R , and thus would be excluded from our analysis. Instead the other one crosses the horizontal line quite close to the cluster center and in a point with $R > 0$, so could contain an actual structure falling toward the cluster.

Matching these three selection methods, we end with overdensities that should represent the physical process we want to explore.

3.3 Mass and orientation

Having identified a sheet around a cluster, it is possible to extract the cluster mass using the standard Monte Carlo (MC) fitting methods. In particular, we apply the Monte Carlo Markov Chain (MCMC) to the galaxies belonging to every sheet.

The code we use for this analysis is from Falco et al. (2014) ^[20].

The Monte Carlo methods are a family of probabilistic methods that can be used to solve elaborate problems by exploring the parameter space, even in high-dimensional problems. These methods make use of random numbers to extract a sample from a large system, choosing it in a way so that it will be representative of the entire system.

Taking random steps led by a probability function, this technique goes around in the parameter space and decides whether to accept the step or not to by evaluating its probability: if it's higher than the probability of the current position, the step is taken, otherwise the step can be accepted with probability $P(new)/P(old)$.

This jumping process is called *Markov Chain* and describes a random path where the probability distribution at each step only depends on the present position and not on the way we arrived there. The guide for the random steps is the likelihood function.

This chain starts from a point set by the user, and then the algorithm runs for several steps until the initial state is forgotten. These initial points, called burn-in, are usually discarded and after them the chain approaches a stationary distribution where the set of accepted values represents a sample from the probability distribution. The quality of the sample improves as a function of the number of steps.

The great convenience of the MC methods is that we can include a lot of parameters even with a quite small computational time.

In our case, we run 5000 combinations of parameters and then remove the burn-in points. The likelihood used for this analysis is:

$$\mathcal{L}(\alpha, M_v | v_{los}) = \prod_{i=1}^N \exp \left(-\frac{(v_{los i} - v_{los model}(R_i))^2}{2\sigma^2} \right),$$

where the model is given by equation (3.3) and the free parameters are α and M_v . We set $\Delta = 93.8$ and $H_0 = 73$ km/s/Mpc, as these are the values set in the cosmological simulation used to test the method.

The scatter of the model, indicated as σ in the likelihood expression, is fixed for every sheet and it's evaluated by measuring the velocity dispersion of the sheet in the (R, v_{los}) space. This velocity dispersion results from a combination of the radial and the tangential velocities.

The MCMC analysis gives us the resulting value for the virial mass and for the three-dimensional angle of the sheet, with their errors.

The value obtained for the orientation α of a sheet corresponds to the mean angle of all the galaxies in the sheet. However we can use it to calculate the corresponding coordinate along the line of sight for all the galaxies and thus to reconstruct a 3D map of the structures we find.

Chapter 4

Results on cosmological simulation

As in Falco et al. (2014), we first test the method on cluster-size halos from a cosmological N-body simulation of pure Dark Matter (DM). The simulation is based on the 3-year Wilkinson Microwave Anisotropy Probe (WMAP3) cosmology.

The cosmological parameters are $\Omega_m = 0.24$ and $\Omega_\Lambda = 0.76$, and the reduced Hubble parameter $h = 0.73$. The particles are confined in a box of size $160 h^{-1}$ Mpc. There are 1024^3 particles in the box each one with mass $3.5 \cdot 10^8 M_\odot$. The evolution is followed from the initial redshift $z = 30$ using the MPI version of the ART code ^[32] ^[26]. The algorithm used to identify clusters is the hierarchical friend-of-friends (FOF) with a linking length of 0.17 times the mean inter-particle distance. The cluster centers correspond to the positions of the most massive substructures found at the linking length eight times shorter than the mean inter-particles distance. The virial radius of the haloes is defined as the radius containing an overdensity of $\Delta = 93.8$ relative to the critical density of the Universe ^[57].

We apply the method on four simulated haloes selected at redshift $z = 0$ with the virial quantities shown in Tab. 4.1:

halo	number of particles	M_v [$10^{14}M_\odot$]	r_v [Mpc]	V_v [km/s]
29	723 618	2.516	1.630	815.117
30	673 289	2.341	1.592	795.766
42	382 480	1.330	1.318	659.068
50	498 399	1.733	1.440	719.858

Table 4.1: Haloes from a N-body simulation used as test for the method

These four halos have been chosen because of the richness of their outskirts, in order to have a good sample to start testing the method.

We treat the DM particles in the haloes as galaxies from observations, so the first step is to project the three-dimensional haloes in 2D, as we would see them on the sky. We consider the z direction as possible line of sight, and we account the galaxies in the box $x = [-20, 20]$ Mpc and $y = [-20, 20]$ Mpc centered on the halo, where x and y are the two directions perpendicular to the line of sight. We assume that the infall velocity profile for the DM particles is the same as the infall profile for galaxies, assumption justified by the fact that the bias resulting from this approach is not expected to be significant. In fact, it has been shown that the ratio of the galaxy velocity dispersion to that of the DM particles in cosmological simulations is likely to be very small ($b_v \approx 1$) ^[19]. Moreover, it should be even smaller in this work since our analysis extends to regions very far from the halo center.

4.1 Halo 29

Using the method described in section 3.2.2 we identified several structures in the simulated haloes. Consider the halo 29, shown in Fig. 4.1.

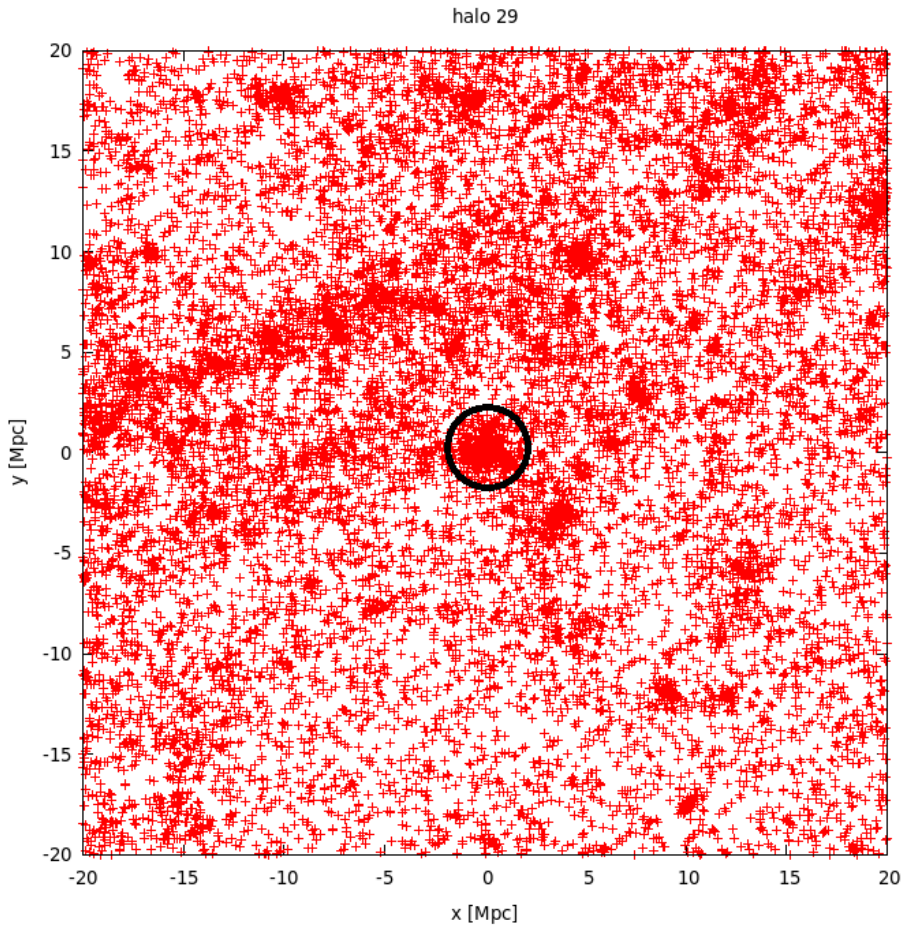


Figure 4.1: Halo 29 projected along the z direction. The black circle shows its virial radius.

The halo is the overdensity we can see in the middle of the plot (its virial radius is 1.630 Mpc), and is surrounded by a large number of structures. However, from this representation it is not clear whether these structures have or not a coherent motion toward the center.

As said before, the first step is to cut the (x, y) plane into 8 two-dimensional wedges, so that we can have a region to analyze and a background one. This cut is shown in Fig. 4.2, where the black points in the middle represent the cluster inside the virial radius, and the two

different colors and symbols are used to distinguish the 8 wedges. The numbers show the numeration used henceforth to discern among the 8 wedges.

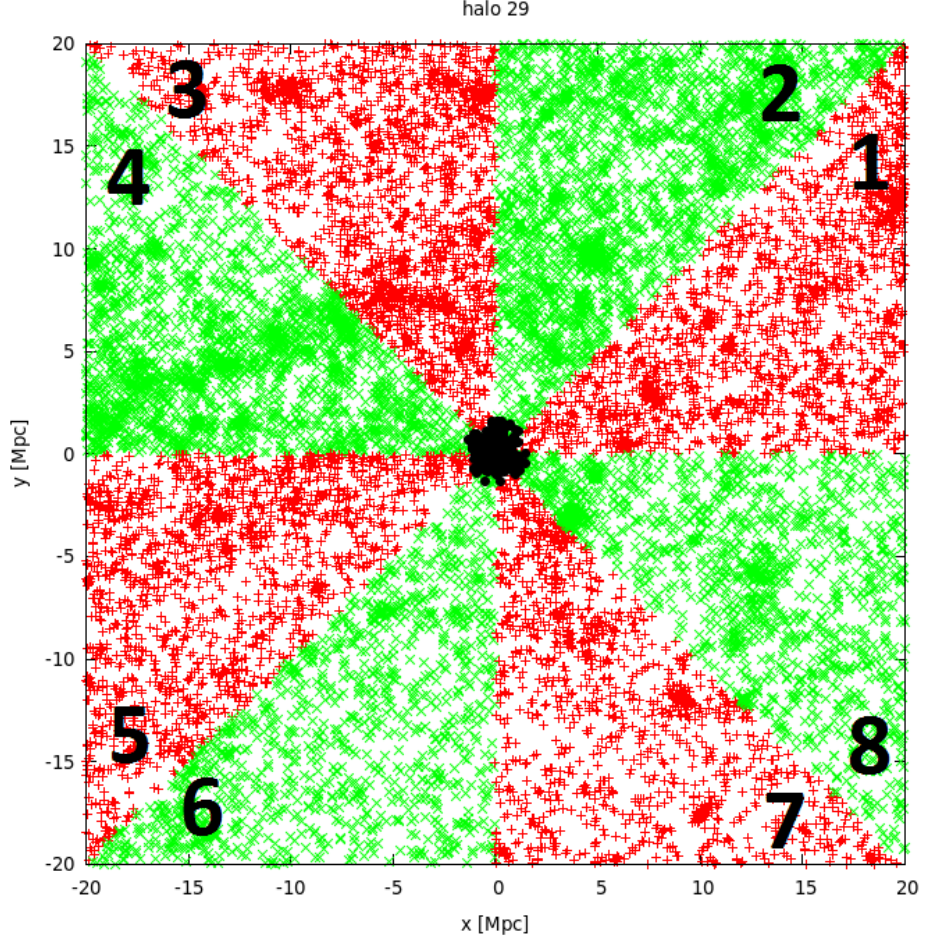


Figure 4.2: The 8 wedges used in the analysis. The red crosses are the particles in the odd wedges, while the green x's are in the even ones.

Now we can analyze each of the selected wedges by looking at them in the (R, v_{los}) space and comparing the galaxy number density with the same quantity in the rest of the wedges, as in equation (3.4). To do this, we take one wedge, for instance the 4th, and we exclude from the background the two adjacent ones, so in this case the 3th and the 5th, as explained before.

Fig. 4.3 shows this selection: the red crosses are the particles in the selected wedge, the green open circles are the ones in the adjacent wedges, so the ones excluded from the analysis, while the green x's are the background we choose.

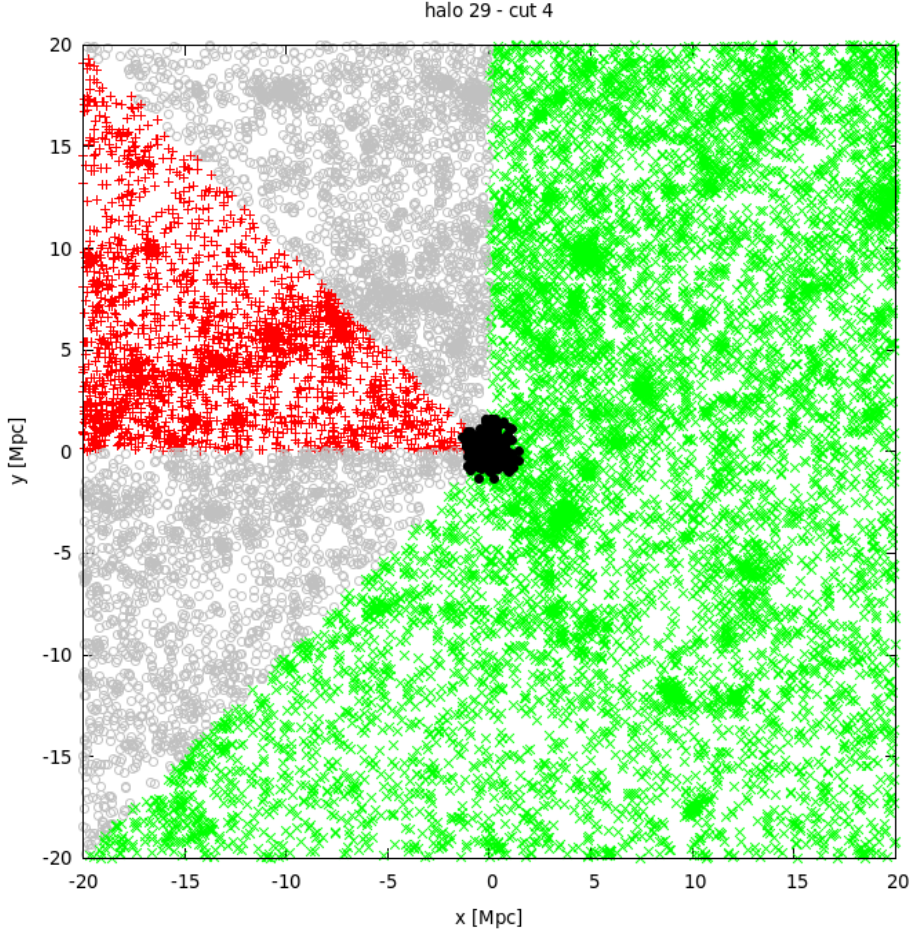


Figure 4.3: Example of signal (red crosses) and background (green x's) regions in the (x, y) plane. The gray open circles are the particles in the excluded wedges.

The identification of the overdensities occurs now in the phase-space, where we build a rectangle around every particle and we count the galaxy number density n_i inside the rectangle. We compare this number with the galaxy number density in the same rectangle but in the background region n_i^{bg} . There is another possibility, that is to use as background the same wedge, considering the rectangle in the opposite side of the (R, v_{los}) plot with respect to the line $v_{los} = 0$. In this way we use the same wedge for the signal and for the background (see Fig. 4.4). We used both these kinds of background, in order to compare the results in the two cases.

In Fig. 4.5 we show this wedge as we see it in the phase-space (top panel) and the background made by the other wedges (bottom panel).

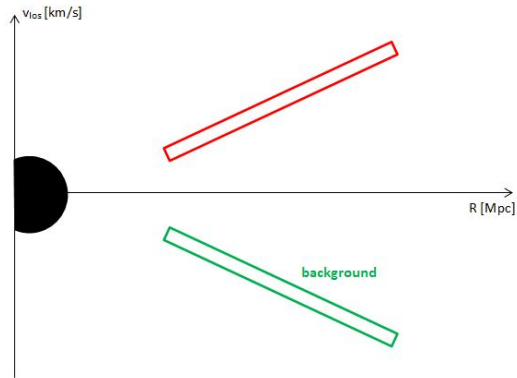


Figure 4.4: Schematic view of the background region if taken from the same cut of the signal region. The rectangle with same R and opposite v_{los} acts as background in this case.

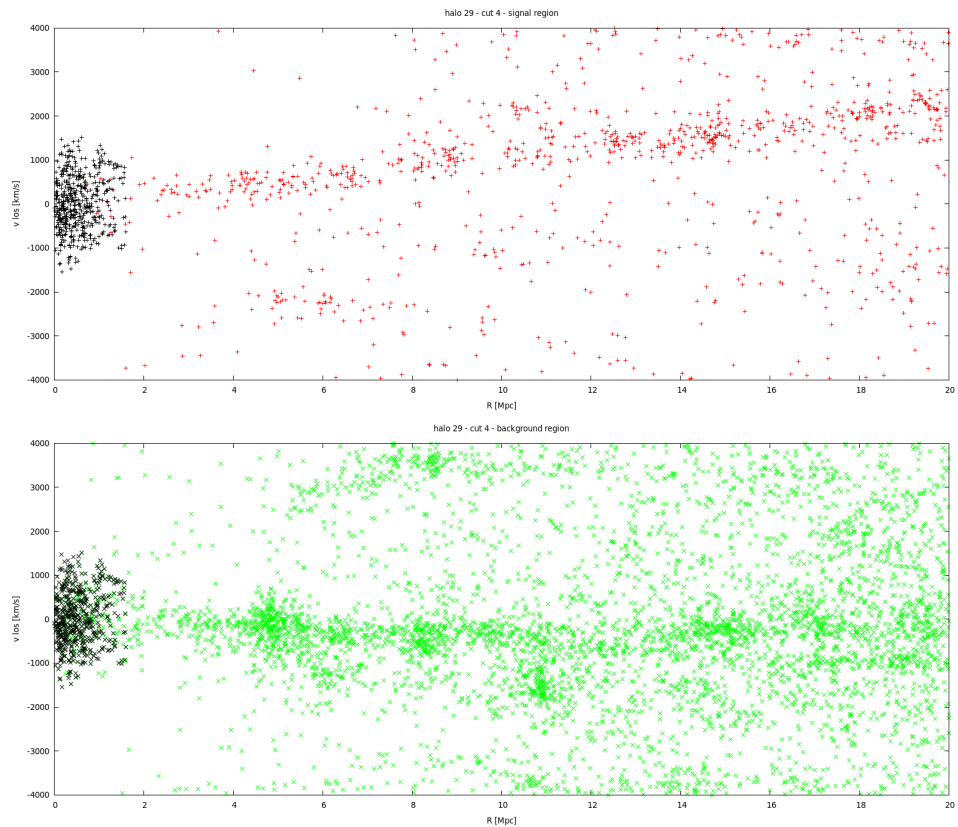


Figure 4.5: (*Top panel*) Wedge 4 in the phase-space. (*Bottom panel*) Background region made by wedges 1-2-6-7-8.

We can now analyze the particles in the wedges and proceed with the analysis described before, that is constructing the rectangles around each particle, evaluating the overdensity, change rectangle, and so on. We also have to select the resulting rectangles using the three criteria based on overdensity and angles distributions and crossing point with $v_{los} = 0$.

In Fig. 4.6 there is an example of how the method works: in the top panel we show all the rectangles that passed the selection criteria, while in the bottom panel we show all the particles inside these rectangles, i.e. the actual overdensity. We will use the (R, v_{los}) coordinates of these particle to reconstruct the infall profile from which obtaining the mass of the halo.

From this figure it is also possible to see the overlapping of the rectangles that yielded to the selection method through the distribution of the rectangles orientations.

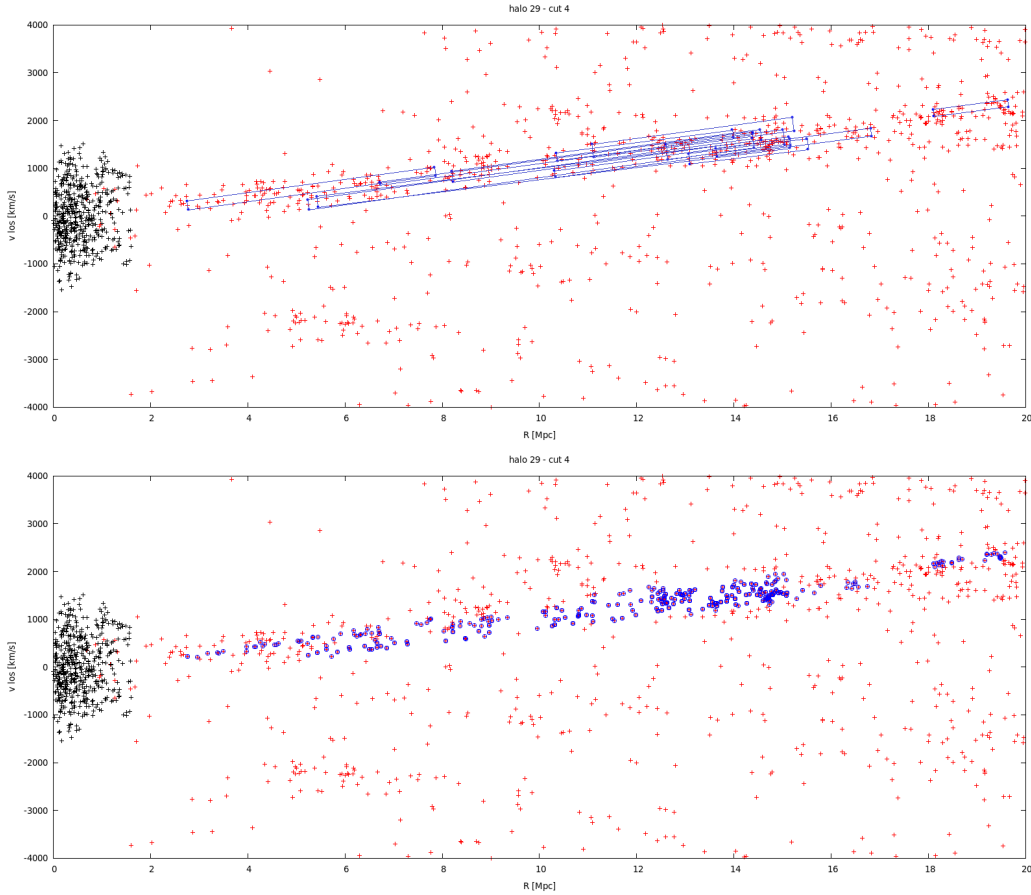


Figure 4.6: (*Top panel*) Final rectangles for the 4th wedge. (*Bottom panel*) Galaxies belonging to the rectangles and forming the overdensity.

The resulting mass given by this overdensity is $2.30 \cdot 10^{14} M_\odot$ with a 2σ uncertainty of $\pm 0.68 \cdot 10^{14} M_\odot$, so in very good agreement with the true virial halo mass that is $2.516 \cdot 10^{14} M_\odot$, while for the orientation of the structure we obtained $\cos(\alpha) = 0.51 \pm 0.01$ when the true mean value for these particles angle is $\cos(\alpha) = 0.52$.

From the cosine of the angle we extract α by inverting the function, while σ_α has been computed through the propagation of uncertainty, so:

$$\begin{aligned} \sigma_\alpha &= \left| \frac{\partial \arccos(\cos(\alpha))}{\partial \cos(\alpha)} \sigma_{\cos(\alpha)} \right| \\ &= \frac{1}{\sqrt{1 - \cos^2(\alpha)}} \sigma_{\cos(\alpha)}. \end{aligned}$$

Fig. 4.7 shows the result of the Monte Carlo analysis, with the scatter plot of the two free parameters ($\cos(\alpha)$, M_v) and the two histograms which represent the probability density function of these two parameters.

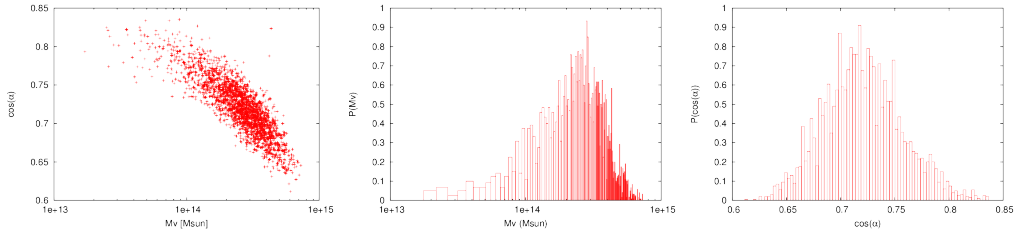


Figure 4.7: Result of the MCMC applied to the sheet in the 8th wedge

In this halo we found other two overdensities, and the results for mass and orientation are listed in the following table.

HALO 29 - $M_v = 2.516 \cdot 10^{14} M_\odot$						
cut	M_v [$10^{14} M_\odot$]	σ_M [$10^{14} M_\odot$]	$\cos(\alpha)$	$\sigma_{\cos(\alpha)}$	α [rad]	σ_α [rad]
4	2.30	0.91	0.51	0.01	1.04	0.01
7	4.15	2.21	0.74	0.02	-0.74	0.04
8	2.82	0.95	0.72	0.04	-0.76	0.06
mean value for the mass: $(2.68 \pm 0.63) \cdot 10^{14} M_\odot$						

One of the three sheets we have in this halo (wedge 4) is behind it (so with positive v_{los} and α) while the other two (wedges 7 and 8) are between the halo and us (so with negative v_{los} and α); we find them with both kinds of background.

Fig. 4.8 shows the results for the mass normalized to the true value of the halo virial mass, while the corresponding overdensities are in Fig. 4.9.

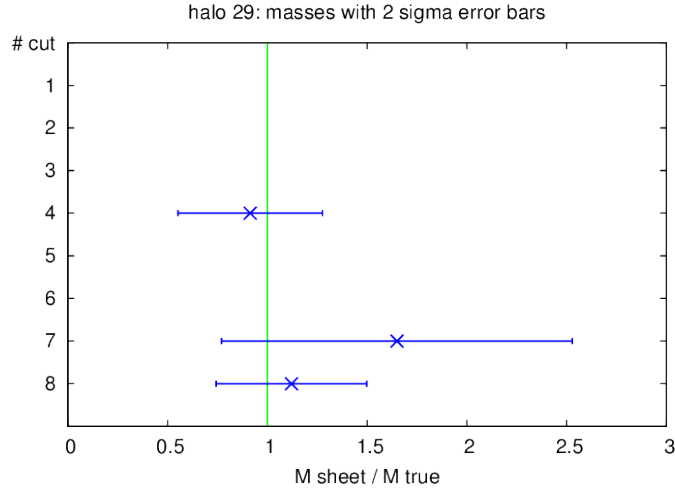


Figure 4.8: Masses with 2σ errors obtained from the sheets normalized to the true value of the halo mass (halo 29).

From Fig. 4.9 we can see how different the sheets can be for length, width and orientation; in general we saw that the more the overdensity is thin and elongated, the more accurate is the result of the mass.

If we take for example the wedge 7, we notice that the overdensity in it is very disperse and thick, and even not very oblique. The resulting mass is actually the worst estimation we have for this halo. The value of the mass is still correct within 2σ , but the error is much larger, and the central value quite far from the real one. If we now look at the best estimation we have, that is given by the overdensity in wedge 4, we have a first confirmation of the fact we mentioned, that is this tendency of long, thin overdensity to give better results for the mass.

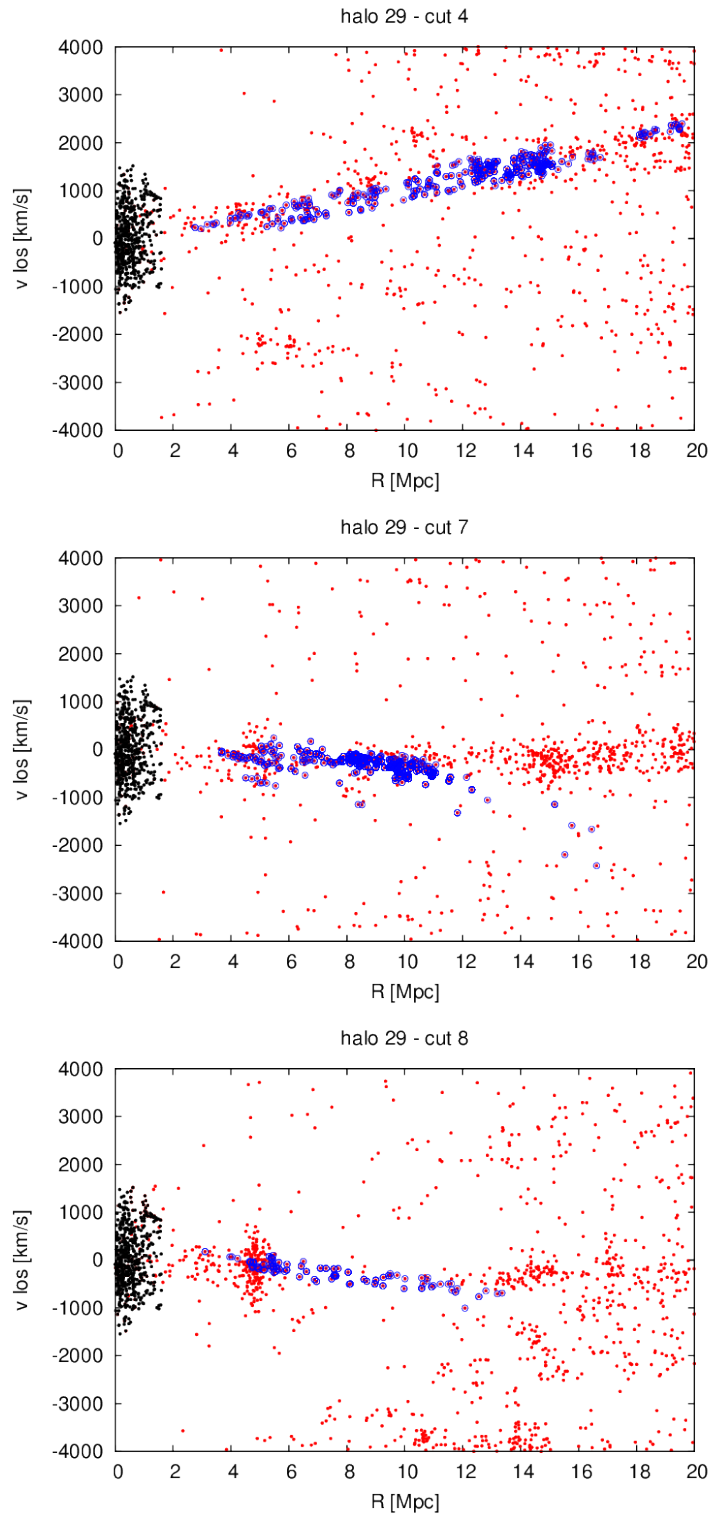


Figure 4.9: Sheets in three wedges of halo 29.

4.2 Halo 30

We carried out the same steps for the other simulated halos.

The results we obtained for mass and orientation are listed in the following table with their 2σ errors.

HALO 30 - $M_v = 2.341 \cdot 10^{14} M_\odot$						
cut	M_v [$10^{14} M_\odot$]	σ_M [$10^{14} M_\odot$]	$\cos(\alpha)$	$\sigma_{\cos(\alpha)}$	α [rad]	σ_α [rad]
1	3.77	1.86	0.68	0.04	0.82	0.06
2 ⁽¹⁾	2.55	1.47	0.34	0.02	1.23	0.02
2 ⁽²⁾	2.63	1.70	0.33	0.07	-1.24	0.07
mean value for the mass: $(2.90 \pm 0.95) \cdot 10^{14} M_\odot$						

They are in good agreement with the true value of the mass as we can see in Fig 4.10, and again the best estimation is given by the most thin and definite overdensity (central panel in Fig. 4.11).

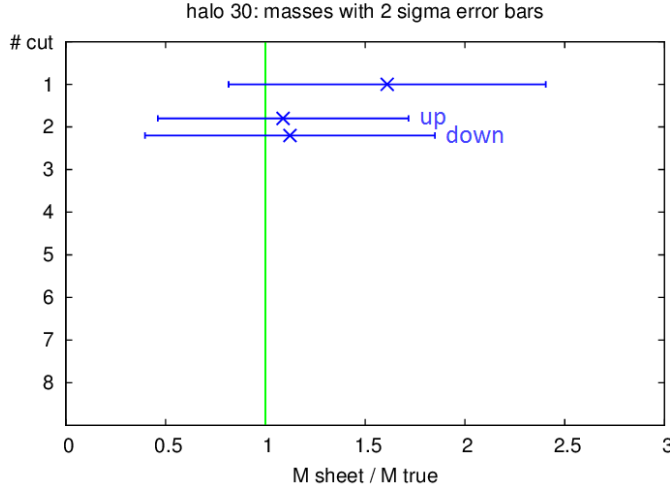


Figure 4.10: Masses with 2σ errors obtained from the sheets normalized to the true value of the halo mass (halo 30).

In this halo we found two overdensities in the same wedge, one behind the halo (central panel in Fig. 4.11), the other one between the halo and us

(bottom panel in Fig. 4.11). This doesn't affect our analysis because the two structures are treated separately, and the fact that we see them in the same cut is just a projection effect.

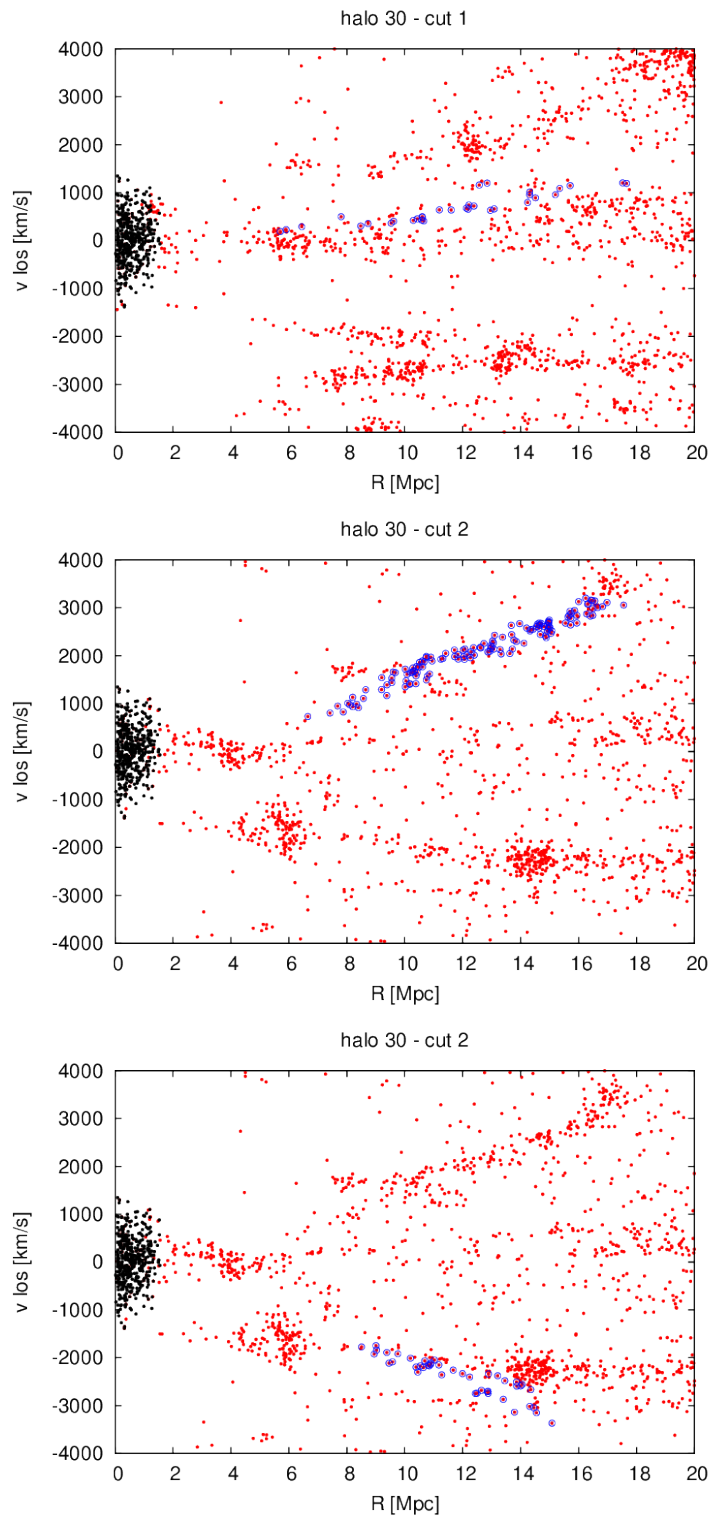


Figure 4.11: Sheets in three wedges of halo 30.

4.3 Halo 42

In order to prove that our method is independent on the projection of the cluster, for halo 42 we consider both the z -projection (as we did for the previous ones) and the x -projection, with the results shown in the following table.

HALO 42 - $M_v = 1.330 \cdot 10^{14} M_\odot$						
cut	M_v [$10^{14}M_\odot$]	σ_M [$10^{14}M_\odot$]	$\cos(\alpha)$	$\sigma_{\cos(\alpha)}$	α [rad]	σ_α [rad]
2 ⁽¹⁾	2.77	1.49	0.31	0.07	1.26	0.07
2 ⁽²⁾	2.63	2.06	0.54	0.17	-1.00	0.20
3	1.52	1.06	0.42	0.04	1.14	0.04
4	1.64	1.26	0.46	0.02	-1.09	0.02
mean value for the mass: $(1.93 \pm 0.67) \cdot 10^{14}M_\odot$						

HALO 42 (x projection) - $M_v = 1.330 \cdot 10^{14} M_\odot$						
cut	M_v [$10^{14}M_\odot$]	σ_M [$10^{14}M_\odot$]	$\cos(\alpha)$	$\sigma_{\cos(\alpha)}$	α [rad]	σ_α [rad]
4	1.86	1.38	0.51	0.01	1.04	0.01
5	1.42	1.21	0.54	0.01	1.00	0.01
6	3.97	3.62	0.64	0.13	-0.88	0.17
8	1.82	1.20	0.69	0.09	0.81	0.12
mean value for the mass: $(1.76 \pm 0.71) \cdot 10^{14}M_\odot$						

We can see that within the uncertainties the method works for both the projections without significant differences.

Figs. 4.12 and 4.13 show the normalized results for the two projections of the halo.

These plots point out even more the different results among the sheets, and also here we can see from Fig. 4.14 how the sharpness of a sheet affects the corresponding value for the mass.

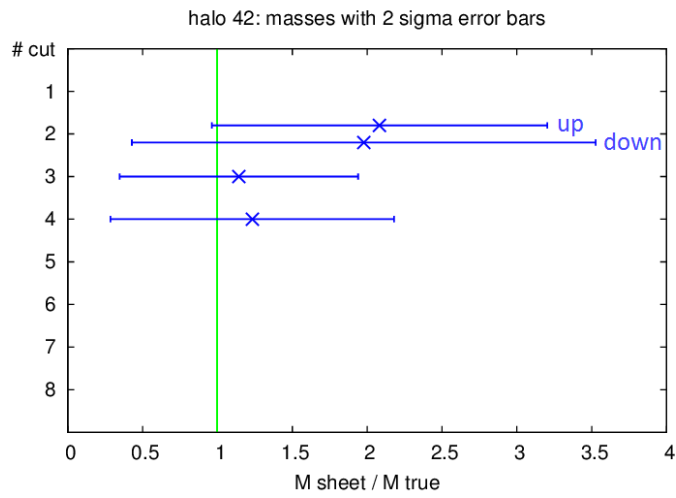


Figure 4.12: Masses with 2σ errors obtained from the sheets normalized to the true value of the halo mass (halo 42).

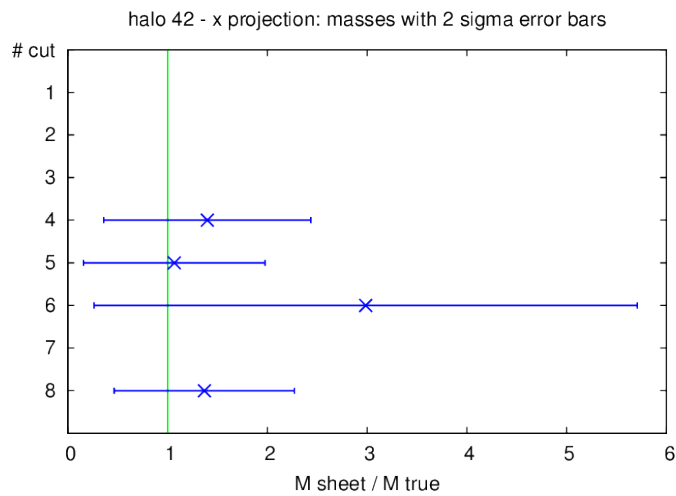


Figure 4.13: Masses with 2σ errors obtained from the sheets normalized to the true value of the halo mass (halo 42, x projection).

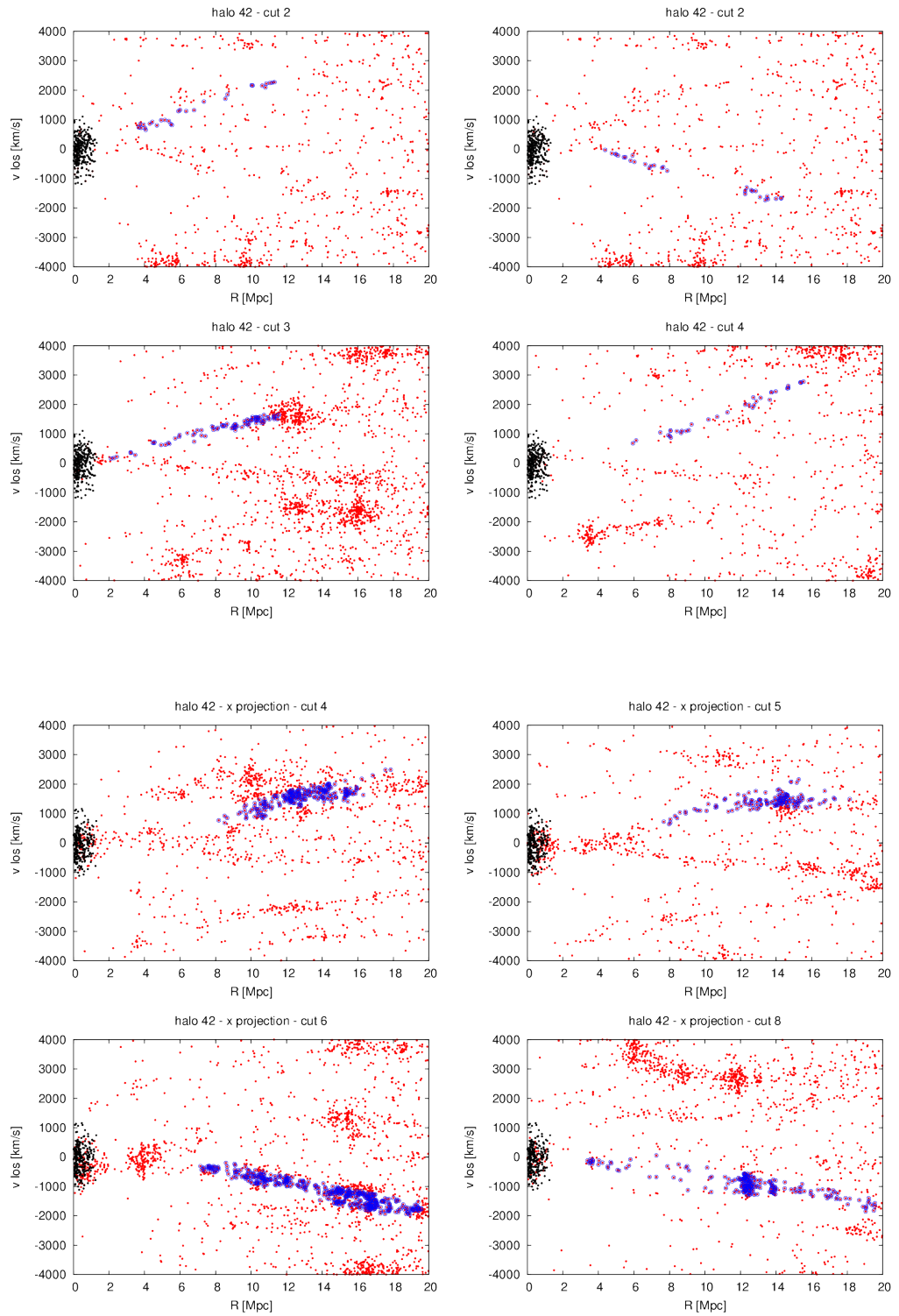


Figure 4.14: Sheets in halo 42.

4.4 Halo 50

In halo 50 we found three different sheets, which gave for the mass the results listed below and shown in Fig. 4.15:

HALO 50 - $M_v = 1.733 \cdot 10^{14} M_\odot$						
cut	M_v [$10^{14} M_\odot$]	σ_M [$10^{14} M_\odot$]	$\cos(\alpha)$	$\sigma_{\cos(\alpha)}$	α [rad]	σ_α [rad]
1 ⁽¹⁾	1.68	1.30	0.40	0.25	-1.16	0.27
1 ⁽²⁾	2.91	1.70	0.73	0.07	-0.75	0.10
3	3.59	2.22	0.69	0.09	0.81	0.12

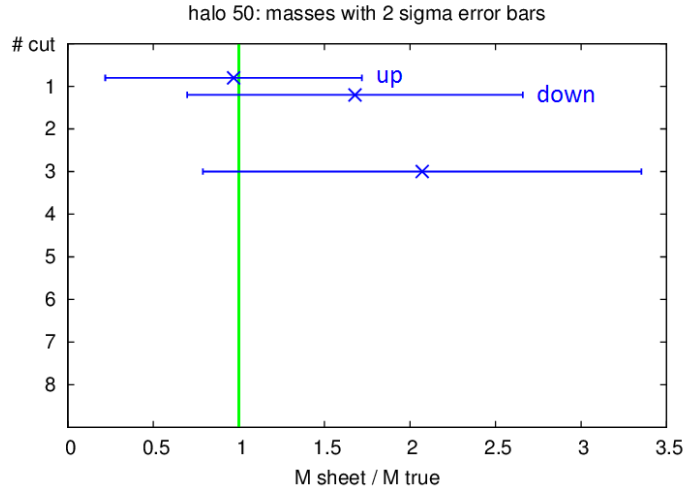


Figure 4.15: Masses with 2σ errors obtained from the sheets normalized to the true value of the halo mass (halo 50).

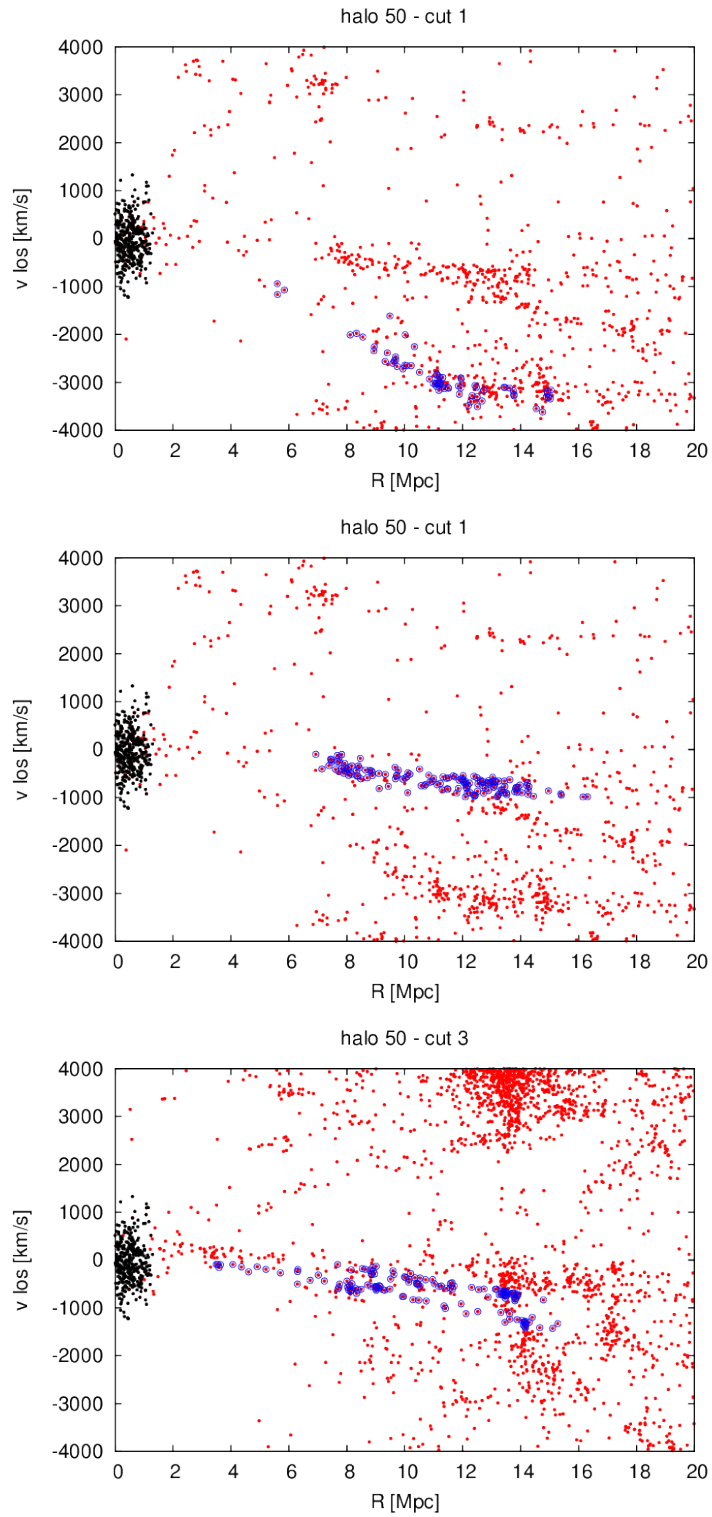


Figure 4.16: Sheets in three wedges of halo 50.

4.5 Discussion

With this method we identify a total of 17 sheets in the four halos we analyzed, with a remarkable improvement in the detection of these structures compared to the method used by Falco et al. (2014).

The mass measurements that our sheets led are generally in very good agreement with the corresponding true masses, confirming that this kinematical analysis can efficiently be used to measure the virial mass of a halo, and also the orientation angle of the sheets is inferred with good accuracy. We obtain the same sheets with the two kinds of background; usually the ones obtained using the same cut as background look a bit more definite, but the estimation of mass and orientation of the sheet is very similar (see Fig. 4.17).

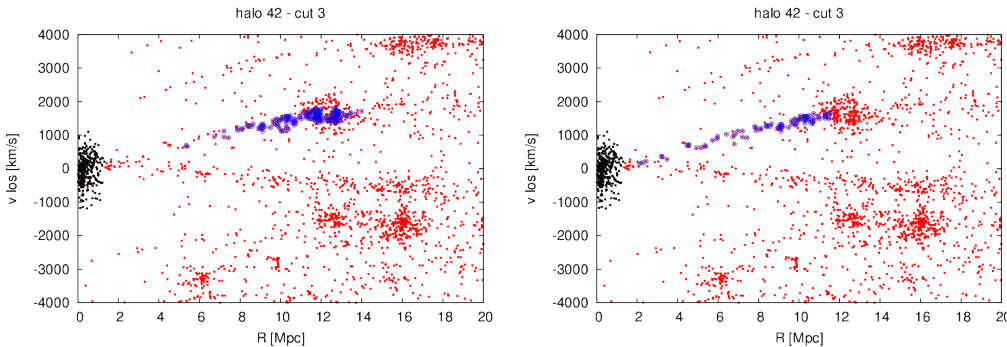


Figure 4.17: Same sheet found outside halo 42 with two different backgrounds: from the other wedges (*left*) and from the same one (*right*).

As in Falco et al. (2014), the method seems to be more sensitive to sheets which are inclined with an angle not bigger than $\alpha \sim 2/3\pi$ with respect to the sky plane, i.e. closer to be faced-on.

We can also note that our method usually tends to overestimate the true value of the mass, even though it is correct within the errors.

A possible source of uncertainties could reside in the assumption of universality of the infall velocity profile. Falco et al. (2014) try to replace the median radial velocity of the three samples they analyze with the fit to the real radial velocity profile of the halo. This gives them an improvement in the estimation of the mass.

By looking at the real infall profile for one of the sheets in our simulated halos (see Fig. 4.18), we find that the universal profile fits quite well the actual one, so that the analysis performed shouldn't be very affected by the approximation used.

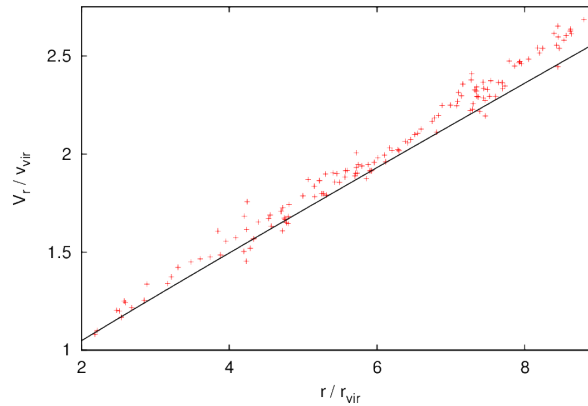


Figure 4.18: Real infall velocity profile for a sheet in halo 30 (wedge 2) compared to the universal fit (black line)

Though, the little shift we observe could be the source of the overestimation we usually find in the mass values; we tried to correct this effect (that is possible only for simulated samples in which we have the real positions and velocities of all the particles) in order to compare the results in the mass estimation.

Fig. 4.19 shows the fit to the real infall velocity profile.

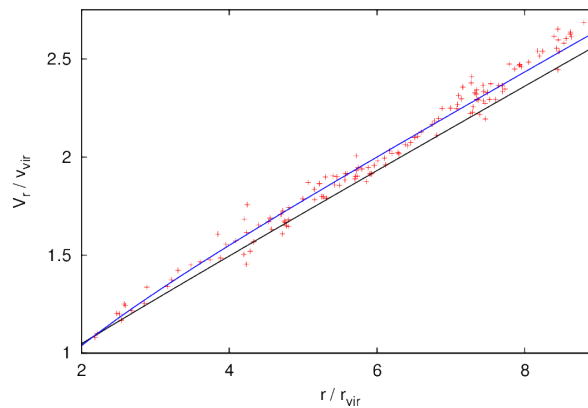


Figure 4.19: Fit to the real infall velocity profile (blue line) for a sheet in halo 30 (wedge 2) compared to the universal fit (black line).

The fit has been performed using eq. (3.3) and the parameter obtained instead of the universal ones are:

$$\begin{cases} a = 1.00 \\ b = 0.99. \end{cases}$$

Using the real profile we obtain the mass and angle estimations shown in the following table.

HALO 30 - $M_v = 2.341 \cdot 10^{14} M_\odot$						
wedge 2 - sheet with $\alpha = 1.21$ rad						
	M_v	σ_M	$\cos(\alpha)$	$\sigma_{\cos(\alpha)}$	α	σ_α
	[$10^{14} M_\odot$]	[$10^{14} M_\odot$]			[rad]	[rad]
universal profile	2.55	1.47	0.34	0.02	1.23	0.02
real profile	2.36	0.79	0.34	0.02	1.23	0.02

So there is an actual improvement using the real infall profile, and the correction of this effect is one of the aims to improve our method.

After this test on simulated halos, we can now try to apply it to a real cluster; the analysis and the results we obtain are presented in the following chapter.

Chapter 5

Results on Coma cluster

The Coma galaxy cluster (*Abell 1656*) is a very studied system of galaxies, as it's the most regular, rich and well observed one in our neighborhood. Its galaxies are mostly elliptical and lenticular with just a few younger spirals, as typical for this kind of rich galaxy clusters.

The Coma cluster is one of the systems where for the first time were observed gravitational anomalies which were considered indicative of an unknown kind of mass. In 1933 Zwicky showed that the galaxies in the cluster were moving too fast for the cluster to be bound together by the visible matter of its galaxies only. Today it is believed that about 90% of the mass of the Coma cluster is in the form of Dark Matter.

Its two brightest members are NGC 4889 and NGC 4874, two giant elliptical galaxies at least 2 or 3 times larger than the Milky Way, well visible at the center of Fig. 5.1.



Figure 5.1: Optical image of the Coma cluster [image from HST].

The Coma cluster has been studied in several wavelengths, from radio to X-rays, in order to characterize its properties. All the mass estimation methods we discussed in chapter 2 have been applied to it, and the results of these studies are listed in Tab. 5.1, where M_{100} corresponds to a density contrast $\Delta = 100$ while M_{200} corresponds to $\Delta = 200$.

method	M [$10^{14}M_{\odot}$]	
Virial theorem	$M_v = 9.5 \pm 1.5$	[55]
X-ray hot gas emission	$M_v = 13 \pm 2$	[29]
Dynamical analysis	$M_{100} = 15 \pm 4.5$	[37]
Caustic method	$M_{200} = 15 \pm 4.1$	[24]
Weak lensing	$M_{200} = 18.8^{+6.5}_{-5.6}$	[33]
Sheets	$M_v = 9.2 \pm 2.4$	[20]

Table 5.1: Coma cluster mass estimation

We can note that there is a quite large uncertainty about the mass of Coma, and that the method applied by Falco et al. (2014) tends to underestimate the Coma virial mass compared with previous measurements which either assume equilibrium or sphericity.

However, they based their analysis only on the two sheets they found in the outskirts of the cluster. We try to apply the method using the rectangle selection hoping to find more structures and thus have a more accurate analysis.

5.1 The sample

Using the SDSS data base we apply our analysis to the system. We take as the center of the cluster the galaxy NGC 4874 ^[31], whose coordinates are:

$$\begin{cases} RA = 12^h 59^m 36^s \\ DEC = +27^\circ 57' 33'' . \end{cases}$$

We select galaxies within 18° from the position of the center corresponding to approximately 20 Mpc, with velocities between 3000 and 11000 km/s. The sample contains 9000 galaxies (see Fig. 5.2).

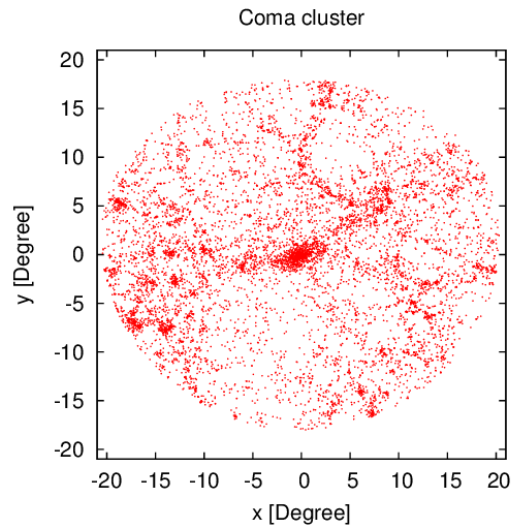
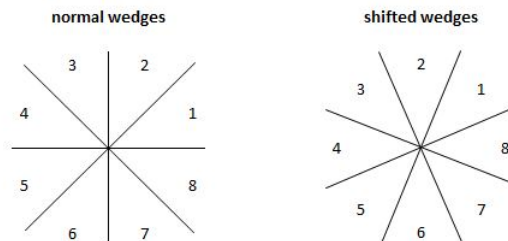


Figure 5.2: Map of the Coma galaxy cluster with its outskirts.

We cut this sample in the usual 8 wedges to analyze them separately, and then we shift this division in order not to lose structures that could eventually lie on the intersection between two wedges (see the scheme below). For each of these configurations we apply the method as we did on the simulations, searching for filaments in the phase-space.



5.2 Identification of the sheets

We apply the rectangle method for each wedge using both kinds of background and in the two different wedge configurations. The structures we found are shown in Fig. 5.3.

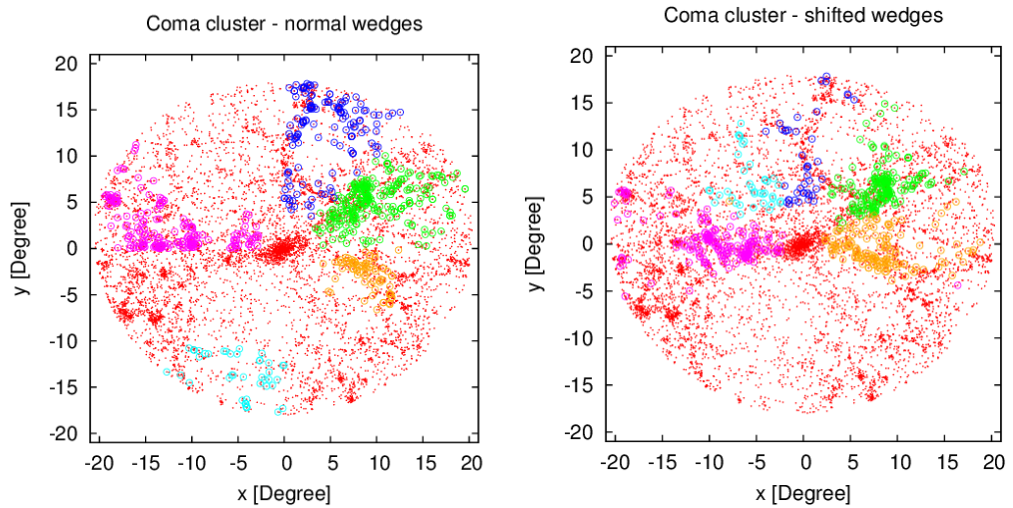


Figure 5.3: Structures outside Coma galaxy cluster

We can see that with one exception (light blue structure) we found the same sheets in both configurations. In Fig. 5.4 there are the same structures as we see them in the phase-space, where the identification occurs. The left panels correspond to the normal wedges while the right ones correspond to the shifted ones. The colors are the same we used in Fig. 5.3.

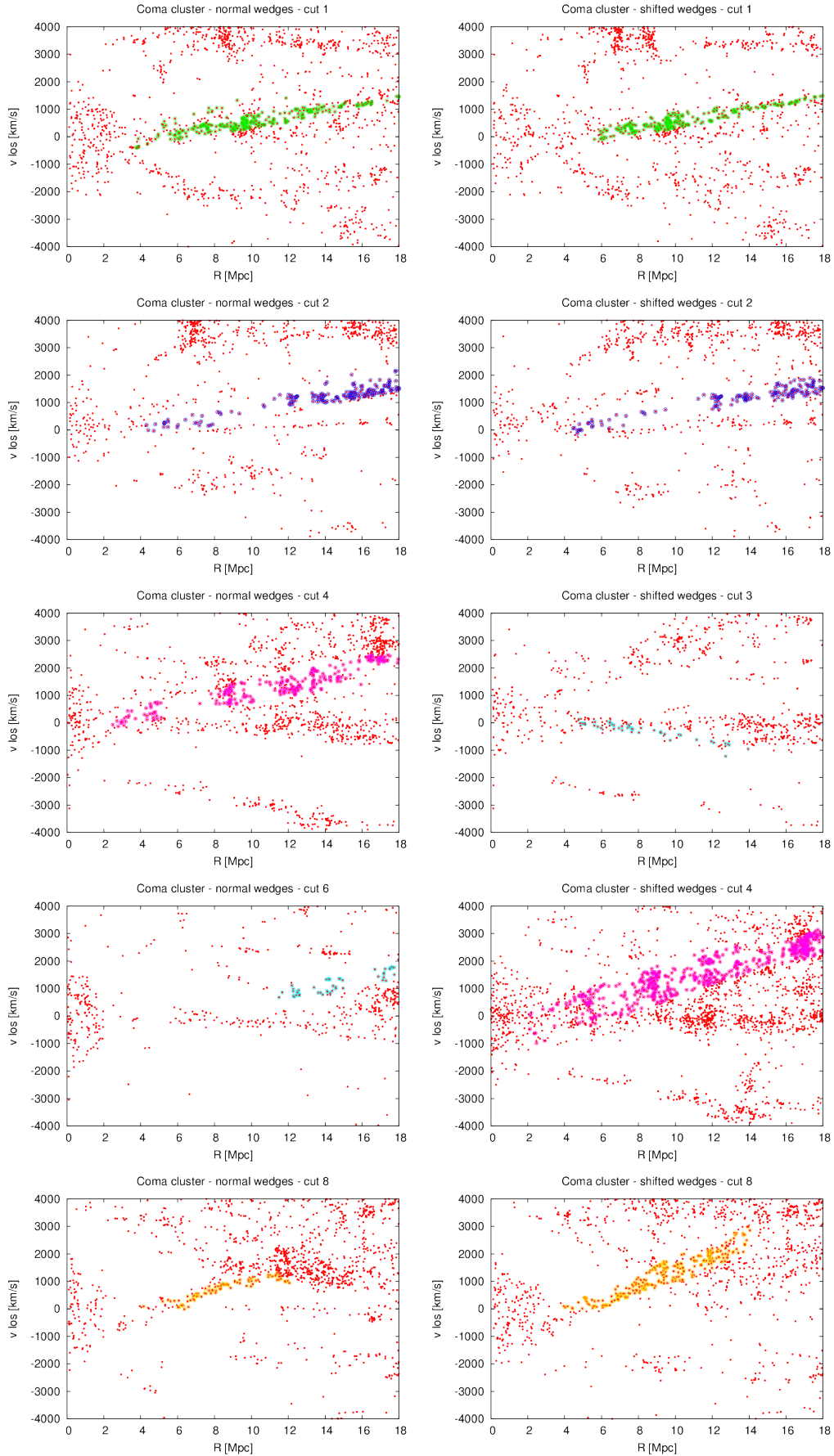


Figure 5.4: Sheets outside Coma.

5.3 Analysis and results

The sheets shown in the previous section are now used to infer the total mass of Coma by the Monte Carlo analysis. The results are shown in Tab. 5.2 for the usual kind of wedges and in Tab. 5.3 for the shifted ones.

Coma cluster - normal wedges						
cut	M_v [$10^{14}M_\odot$]	σ_M [$10^{14}M_\odot$]	$\cos(\alpha)$	$\sigma_{\cos(\alpha)}$	α [rad]	σ_α [rad]
1	6.75	1.89	0.62	0.02	0.90	0.02
2	5.28	2.71	0.56	0.01	0.97	0.01
4	9.49	1.09	0.45	0.01	1.10	0.01
6	8.97	5.32	0.58	0.03	0.96	0.04
8	12.01	5.83	0.46	0.03	1.09	0.03
mean value for the mass: $(8.36 \pm 0.85) \cdot 10^{14}M_\odot$						

Table 5.2: Mass and angles for normal wedges

Coma cluster - shifted wedges						
cut	M_v [$10^{14}M_\odot$]	σ_M [$10^{14}M_\odot$]	$\cos(\alpha)$	$\sigma_{\cos(\alpha)}$	α [rad]	σ_α [rad]
1	11.37	2.96	0.59	0.02	0.94	0.02
2	5.62	2.69	0.56	0.01	0.97	0.02
3	9.40	4.72	0.64	0.06	-0.87	0.08
4	10.16	1.31	0.39	0.01	1.17	0.01
8	12.24	2.86	0.51	0.03	1.04	0.03
mean value for the mass: $(9.89 \pm 1.00) \cdot 10^{14}M_\odot$						

Table 5.3: Mass and angles for shifted wedges

We can see how even within the errors each sheet gives a quite different estimation of the mass. We will discuss this discordance in the next chapter. Anyway in some cases there is a very good agreement between the mass and the angle returned from the same sheet in the two different configurations (look for example at the sheets 2 and 8).

All the sheets shown are obtained from taking the background from the same wedge where we look for overdensities, since in this way, as for the simulated halos, the resulting overdensities are much more well defined.

The mean values are also in good agreement with the mass that Falco et al. (2014) ^[20] found with their two sheets (that correspond to sheets 1 and 8 in this work):

$$\begin{cases} M_v = (9.7 \pm 3.6) \cdot 10^{14} M_\odot & \text{sheet 1} \\ M_v = (8.7 \pm 3.3) \cdot 10^{14} M_\odot & \text{sheet 2} \end{cases}$$

that leads to the mean value of $M_v = (9.2 \pm 2.4) \cdot 10^{14} M_\odot$.

We found these mean values using the weighted average of our results:

$$\bar{x} = \frac{\sum_{i=1}^N \frac{x_i}{\sigma_i^2}}{\sum_{i=1}^N \frac{1}{\sigma_i^2}}$$

$$\bar{\sigma} = \sqrt{1 / \sum_{i=1}^N \frac{1}{\sigma_i^2}}$$

Fig. 5.5 shows the masses from the sheets normalized to the mean mass obtained by Falco et al. (2014).

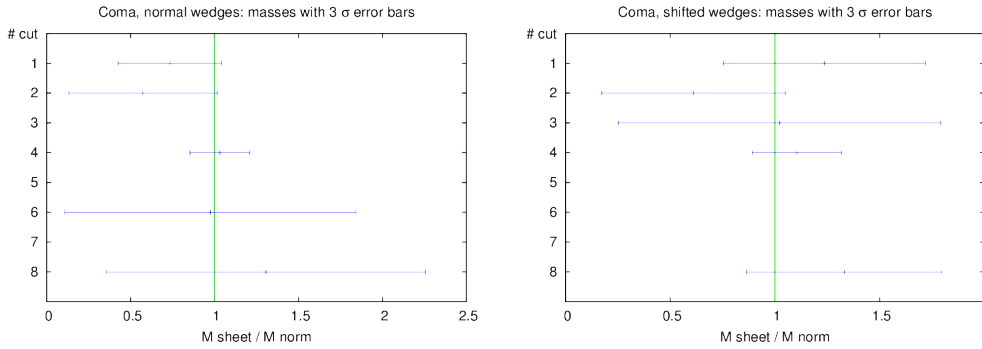


Figure 5.5: Value of the masses obtained from the sheets outside Coma with 3σ error bars. The normalization corresponds to the mean value found by Falco et al. (2014): $M_{norm} = 9.2 \cdot 10^{14} M_\odot$.

Chapter 6

Shape and alignment of galaxy clusters

As we mentioned before, the observations of galaxy clusters show that most of them look elliptical in the sky, even if their 3D structure is usually approximated to a simple spherical model. Moreover, it is believed from both theoretical and observational probes that the best approximation for the shape of galaxy clusters is a triaxial ellipsoid.

From the observational side, the non-circular projection of galaxy clusters emerges in several different analyses: in the optical wavelength, from the density map of galaxy clusters ^[11] [4]; in X-rays, from the surface brightness map ^[35]; in microwaves, from the Sunyaev Zel'dovich pressure map ^[48]; from strong ^[51] and weak ^[44] gravitational lensing; from the azimuthal variation of galaxy kinematics detected recently in a SDSS sample ^[50] where it has been found that the line of sight velocity dispersion of galaxies lying along the major axis of the central galaxy is larger than the one of those that lie along the minor axis.

On the theoretical side, numerical simulations show that haloes form with a triaxial shape, with a preference for prolateness over oblateness ^[3] [23]. Some of these simulations also predict that low mass haloes appear more spherical than high mass ones (even if there are different conclusions in other works ^[47]) and that for a given mass, lower redshift haloes should be more spherical than high redshift ones.

Despite these evidences, the majority of the studies on clusters use the spherical assumption, mainly due to the fact that the quality of the data may not allow a triaxial model to be constrained. However, issues like the mass discrepancy found between, e.g. lensing and X-ray data when spherical symmetry is assumed, suggest the growing need for non-spherical models.

6.1 Effect of asphericity in caustic mass estimates

There are a few works trying to trace the real shape of galaxy clusters, for instance using the caustic technique.

Svensmark et al. (2014) analyze a sample of galaxy clusters generated from cosmological simulations and show how the dynamical mass estimation from the caustic technique depends on the orientation of galaxy clusters with respect to the line of sight. They investigate the effect of spatial anisotropy caused by the elongation of the cluster itself or by the surrounding large scale structures such as filaments, walls and voids. To this purpose, they create three different stacks in order to isolate the morphological features of the halos ^[54]:

- *ellipsoidal stack*: where halos were modeled as ellipsoidal structures and rotated so that the three principal axes of each halo were aligned;
- *filamentary stack*: where the direction of the largest filament associated with each halo was aligned;
- *spherical stack*: for reference with arbitrary orientation of each halo.

The three configurations made it possible to choose any line of sight through the anisotropic stacks and compare mass estimates from caustics with those of the spherical stack. The stacks differ only in the orientation of individual halos, so they have the same true cumulative mass profile $M(< r)$, and thus any difference in caustic mass estimation between the non-spherical (ellipsoidal and filamentary) stacks and the spherical one expresses an anisotropy bias in the caustic method of mass estimation.

They perform this analysis for two mass bins: one in the range of

$$1 \cdot 10^{14} h^{-1} M_{\odot} < M_v < 2 \cdot 10^{14} h^{-1} M_{\odot} \quad (\text{low-mass bin})$$

which yielded 230 distinct halos in the catalog they use, and the other one in the range of

$$M_v > 2 \cdot 10^{14} h^{-1} M_{\odot} \quad (\text{high-mass bin})$$

which yielded 101 distinct halos.

The results of this work are shown in Tab. 6.1.

mass bin	stack	triaxiality parameter	max/min mass		
		T	1 R_v	2 R_v	3 R_v
low	<i>ellipsoidal</i>	0.69	1.72	1.95	2.44
	<i>filamentary</i>	0.81	1.22	1.49	1.71
	<i>spherical</i>	-	1.03	1.06	1.13
high	<i>ellipsoidal</i>	0.70	2.06	2.22	2.95
	<i>filamentary</i>	0.81	1.21	1.32	1.38
	<i>spherical</i>	-	1.04	1.06	1.11

Table 6.1: Values of triaxiality and mass estimates for the different stacks and mass bins. ^[54]

Here they evaluate the “max/min mass” that is the ratio of the maximum mass estimate to the minimum one they obtained, normalized by the mass of the spherical stack. The triaxiality parameter is defined as follows:

$$T \equiv \frac{a^2 - b^2}{a^2 - c^2},$$

where a , b and c are the three ordered semi-axes of the ellipsoid.

From the values in Tab. 6.1 we can see how the effect is larger for the high mass bin.

The mass estimates achieved in this way can be used to correct the caustic mass estimate when the cluster orientation is known. Even within the virial radius the mass estimates may vary by a factor or ~ 2 for massive clusters.

Svensmark et al. (2014) credit this dependence of the caustic mass on the cluster orientation with respect to the line of sight to the anisotropy of the spatial and velocity distribution of galaxies in clusters. Thus, they expect that this effect is a generic feature of all kinematical methods for the cluster mass determination, such as the methods based on the virial theorem, on the scaling relation between cluster mass and line of sight velocity dispersion, on the Jeans analysis of the velocity moments profiles, on the infall velocity profile like the one described in our work.

However, the discrepancy between the measured and the actual cluster masses may differ among the different methods, so the results they show cannot be regarded as a general prediction for all of them ^[54].

6.2 Combining different data sets

As example of a different way to deduce the shape of a cluster we describe the analysis performed by Limousin et al. (2013) ^[36]. They combine and simultaneously fit X-ray, SZ and gravitational lensing data sets in order to constrain the 3D properties of DM halos and Intra Cluster (IC) gas.

This method is applied to the following clusters: MACS 1423, Abell 1689, Abell 383 and Abell 1835.

Their methodology is based on the fact that both the lensing effect and the X-ray/SZ emission depend on the properties of the DM gravitational potential well, the former being a direct probe of the two-dimensional mass map via the lensing equation, the latter an indirect proxy of the three-dimensional mass profile through the hydrostatic equilibrium equation applied to the gas temperature and density.

In order to infer the model parameters of both the IC gas and the underlying DM density profile, they perform the following steps:

- modeling the DM density using a generalized Navarro-Frenk-White triaxial model:

$$\rho(R) = \frac{\delta_c \rho_{c,z}}{(R/R_s)^\gamma (1 + R/R_s)^{3-\gamma}},$$

where R_s is the scale radius, δ_c is the dimensionless characteristic density contrast with respect to the critical density of the Universe $\rho_{c,z}$ at redshift z , and γ is the inner slope of the density profile ^[30];

- recovering the gravitational potential and two-dimensional surface mass Σ of a DM halo with this triaxial density profile:

$$\Sigma = \int_{-\infty}^{+\infty} \rho(R) dz \quad [40];$$

- solving the generalized hydrostatic equilibrium equation (including the non-thermal pressure) for the density of the intracluster gas

$$\nabla P_{tot} = -\rho_{gas} \nabla \Phi \quad [34] [39]$$

to infer the theoretical three-dimensional temperature profile T ;

- calculating the SZ temperature decrement map

$$\frac{\Delta T(\nu)}{T_{cmb}} = \frac{\sigma_T}{m_e c^2} \int P_e(r) f(\nu; T(r)) dz \quad [36]$$

and the surface brightness map

$$S_X = \frac{1}{4\pi(1+z)^4} \Lambda(T_{proj}^*, Z) \int n_e n_p dz \quad [36]$$

related to the triaxial intracluster medium halo;

- comparing T with the observed temperature, S_X with the observed brightness image, $\Delta T(\nu)$ with the observed SZ temperature decrement, and Σ with the observed two-dimensional mass map, in order to obtain the parameters of the triaxial intracluster medium and DM density model ^[41].

The results of this method are listed in Tab. 6.2.

	Abell 1835	Abell 383	Abell 1689	MACS 1432
c_{200}	4.32 ± 0.44	4.76 ± 0.51	5.27 ± 0.46	3.97 ± 1.0
R_s [kpc]	891.0 ± 114.3	511.2 ± 73.6	683.1 ± 84.7	644.7 ± 162.1
γ	1.01 ± 0.06	1.02 ± 0.06	0.92 ± 0.07	1.06 ± 0.1
$\eta_{DM,a}$	0.59 ± 0.05	0.55 ± 0.06	0.56 ± 0.07	0.62 ± 0.04
$\eta_{DM,b}$	0.71 ± 0.08	0.71 ± 0.10	0.75 ± 0.08	0.72 ± 0.06

Table 6.2: Best-fit model parameters for the four clusters. Error bars correspond to 1σ confidence level. The shown parameters of the DM halos are: c_{200} (concentration parameter), R_s (scale radius), γ (inner DM slope), $\eta_{DM,a}$ (minor-major axis ratio), $\eta_{DM,b}$ (intermediate-major axis ratio). ^[36]

With this analysis combining different kinds of observations they obtain good results in measuring the geometric parameters of galaxy clusters following a triaxial model. A triaxial ellipsoid is still an approximation, since both observations and simulations show for instance the presence of substructures which are not accounted for by a triaxial model for galaxy clusters. If the substructures are small compared to the main cluster halo, then the triaxial approximation may be accurate enough. On the other hand, unrelaxed halos often have shapes that are not adequately described by ellipsoids, making shape parameters ill-defined. Indeed, if there is no clear dominant halo but a superposition of sub-halos with comparable masses, the triaxial approximation may be questionable ^[49]. However, this work constitutes a step forward with respect to the rough spherical analysis.

6.3 Preliminary considerations on the “sheets method”

As we discussed in the previous chapters, the method we use to find the mass of galaxy clusters gives us some not negligible differences in the estimations. We think that these differences could be related to an intrinsic effect and not only to statistical errors.

As Svensmark et al. (2014) pointed out, the mass estimation methods based on kinematical analyses could be influenced by the effect of asphericity of the cluster, giving under or over estimates depending on the alignment of the cluster with respect to the line of sight.

Working on cosmological simulations, for which we know the exact mass and shape of the halo, we also noted this trend: sheets located along the minor axis of the halo tend to give a lower value for the mass than sheets along the major axis.

Besides the uncertainties of the method, we impute this discrepancy to the fact that the cluster is not spherical, so a sheet sited along the minor axis should feel a slightly lower gravitational potential than one sited along the major axis, and so give a lower mass estimation. A different potential leads to a different velocity, that affects the mass estimation in our method; in fact the escape velocity of a gravitationally bound system of particles is related to its gravitational potential by:

$$v_e^2(r) = -2\Phi(r),$$

where r is the distance from the center of the system.

So, if one is able to find at least three sheets oriented along different lines around the cluster, in order to be sure that they don't lie on the same axis of the cluster, it is possible to proceed with this analysis and try to constrain the real shape of the cluster.

As shown before, we find 3 or 4 sheets for each halo we analyzed, so we can try to investigate this aspect.

6.3.1 Looking at simulated halos in 3D

Let’s consider the x -projection of halo 42 where we found 4 well defined sheets. These structures gave us the following results for the mass:

HALO 42 (x projection) - $M_v = 1.330 \cdot 10^{14} M_\odot$						
cut	M_v [$10^{14} M_\odot$]	σ_M [$10^{14} M_\odot$]	$\cos(\alpha)$	$\sigma_{\cos(\alpha)}$	α [rad]	σ_α [rad]
4	1.86	1.38	0.51	0.01	1.04	0.01
5	1.42	1.21	0.54	0.01	1.00	0.01
6	3.97	3.62	0.64	0.13	-0.88	0.17
8	1.82	1.20	0.69	0.09	0.81	0.12

The sheets in wedges 4, 5 and 8 are in very good agreement among them, while the one in wedge 6 returns a quite large overestimation of the real mass, even though the error bar is considerably large.

If we look at this halo (see Fig. 6.1) we can see that it is not spherical, but it’s quite elongated along the y direction.

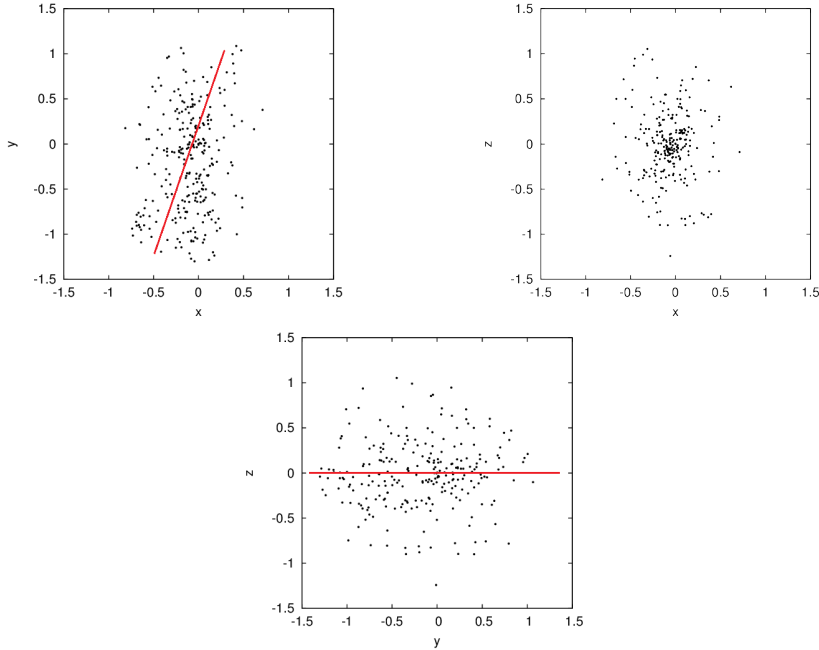


Figure 6.1: Projections of halo 42 inside its virial radius. The red line shows the major axis of the halo.

We plot in Fig. 6.2 the cluster with the surrounding sheets we found before (see Section 3.3).

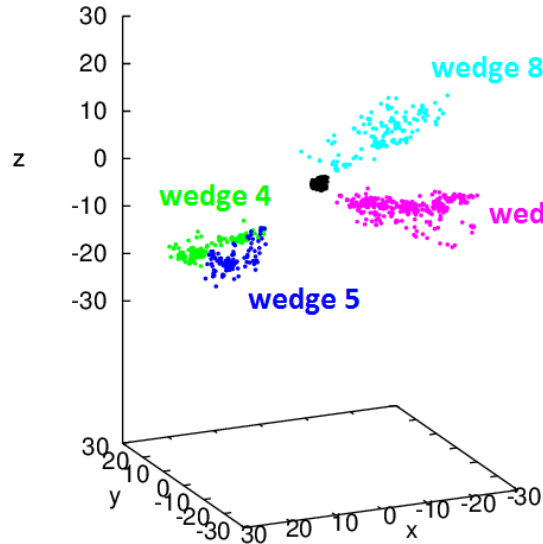


Figure 6.2: Halo 42 with the sheets found in its outskirts.

From the $(x-y)$ projection in Fig. 6.3 we can see that the sheet in wedge 6, that is one with the biggest estimate for the mass, is also the one lying along the major axes of the cluster.

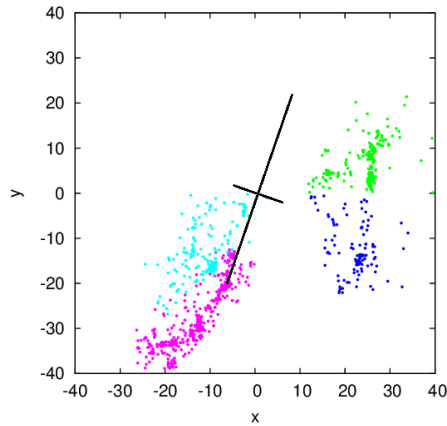


Figure 6.3: $(x-y)$ projection of halo 42 with the sheets surrounding it. The black lines show the direction of the major and minor axes of the halo.

This is a first hint of what we expected, even though it's just a qualitative consideration, but it could be the starting point for a more accurate analysis of this effect.

6.3.2 Color maps

We then try to pursue this aspect by analyzing another halo (#29), that is shown in Fig. 6.4 with an ellipsoidal model to fit its shape.

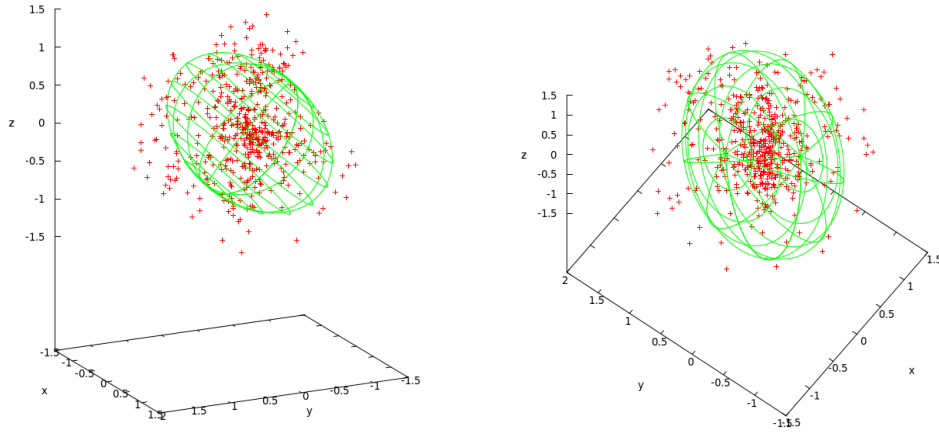
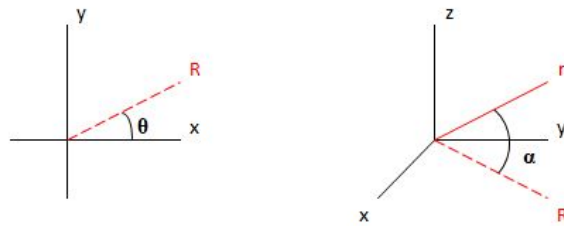


Figure 6.4: 3D view of halo 29 inside its virial radius with the ellipsoidal model that best fit its shape.

We cut the outskirts of the halo in 48 wedges, and in each of them we select a pseudo-sheet in order to apply the mass method estimation and generate a color map, which shows the values of the mass in the (θ, α) distribution, where θ is the angle of the structure in the (x, y) plane and α is the angle between the structure and its projection in the (x, y) plane, i.e. the same angle we find with the MC analysis (see the scheme below).



We do this to see (in a qualitative way) if there are significant differences in the value of the mass, and to possibly relate them to the shape of the halo. The map is shown in Fig. 6.5.

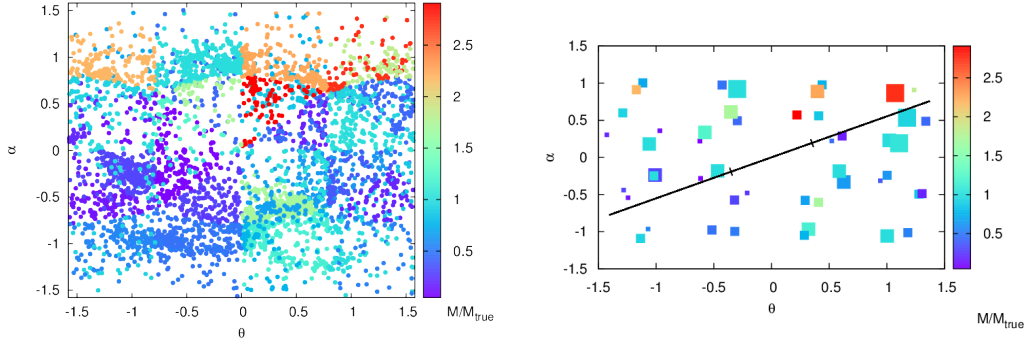


Figure 6.5: Map of the distribution of the halo virial mass found with the MC analysis applied to pseudo-sheets in the surroundings of the halo. (*Left panel*) Each point represents a particle and the color shows the value of the mass normalized to the true virial mass. (*Right panel*) Each square represents a pseudo-sheet with the corresponding value of the mass it returned and the size of the squares is inversely related to the error in the mass estimation. The black line shows the direction of the major axis of the halo.

We clearly see the differences in the mass distribution, up to a factor ~ 3 in the overestimation. To see if there is some kind of correlation between them and the shape of the cluster, in Fig. 6.6 we plot the same map but in the 3 projected planes (x, y) , (y, z) and (z, x) , together with the projection of the halo modeled as in Fig.6.4.

In these three panels we can see an indication that the highest values of the mass actually correspond to the wedges sited along the major axis of the halo (particularly evident in the middle and bottom panels). This can be taken as a further hint of this correlation even if it is again just a qualitative analysis.

However, it could be very interesting to carry on this way of exploring the three-dimensional shape and orientation of galaxy clusters, perhaps with an improvement in the mass estimation method and also supporting this research with a more quantitative approach.

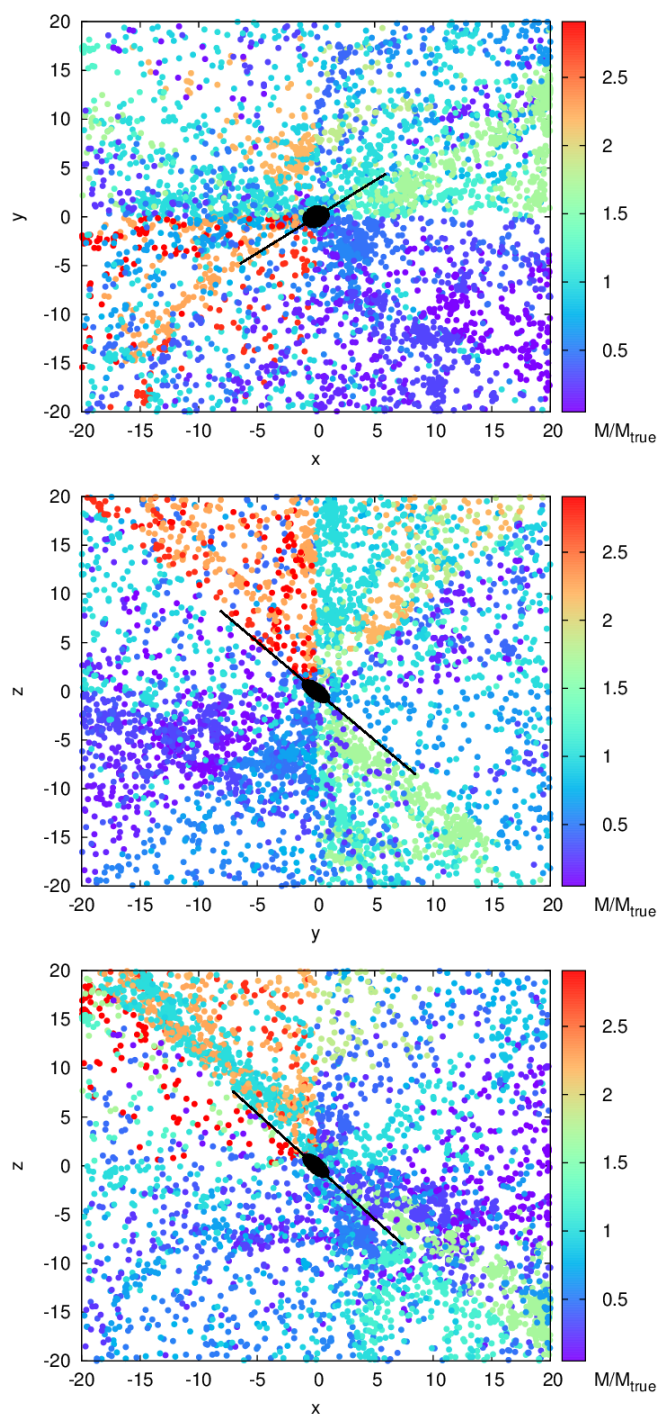


Figure 6.6: Color maps in the three projected planes with the ellipsoid used to model the halo.

Chapter 7

Conclusions

The main purpose of this thesis was to explore the properties of clusters of galaxies, dark matter halos and large scale structures. In particular, we investigated the dynamics of galaxies in the outskirts of clusters, using both a theoretical and observational approach. We proposed a new method for measuring the total mass of galaxy clusters within the virial radius which has been tested on cosmological simulations and then applied to the Coma cluster data. This method involves the detection of extended filaments and sheets, which are typically sitting at 5 – 15 Mpc from the virialized cluster.

The idea is to infer the mass only from the kinematical data of these structures in the cluster outskirts. In the hierarchical scenario of structure formation, galaxy clusters are located at the intersection of filaments and sheets, and the motion of such non-virialized structures is thus affected by the presence of the nearest massive cluster. We found that modeling the kinematic data of these objects leads to an estimation of the neighbor cluster mass. The gravitational effect of the cluster is to perturb the pure Hubble motion of the filaments, leading them to a deceleration, and thus the measured departure from the Hubble flow of those structures allows us to infer the virial mass of the cluster.

We have developed a technique to detect the presence of structures outside galaxy clusters, by looking at the phase space (chapter 3). The proposed technique doesn't aim to map all the objects around clusters, but it is limited to finding those structures that are suitable for the virial cluster mass estimation. Our method doesn't require the dynamical analysis of the virialized region of the cluster, therefore it is not based on the dynamical equilibrium hypothesis. However, it relies on the assumption of spherical symmetry of the system by the fact that we assume a radial velocity profile.

Moreover, our method is biased by fixing the fit to the radial infall velocity profile of simulations, as a universal infall profile.

From the practical point of view, this technique requires gathering galaxy positions and velocities in the outskirts of galaxy clusters, up to few tens of Mpc, and looking for overdensities in the (R, v_{los}) -space that correspond to filaments or sheets. Once a structure is detected, the fit to its line of sight velocity profile has to be performed. The fitting procedure involves only two free parameters: the virial mass of the cluster and the orientation angle of the structure in 3D.

We analysed halos from cosmological simulations first, in order to test both the technique to identify structures outside clusters and the method to extract the cluster mass (chapter 4). We analyzed four halos in which we found a total of 17 sheets and we obtained for these sheets the following values for the mass, normalized to the true halo virial mass:

- halo 29 $\bar{M}/M_{true} = 1.06 \pm 0.25$
- halo 30 $\bar{M}/M_{true} = 1.24 \pm 0.41$
- halo 42 $\bar{M}/M_{true} = 1.44 \pm 0.51$
- halo 42x $\bar{M}/M_{true} = 1.33 \pm 0.53$
- halo 50 $\bar{M}/M_{true} = 1.38 \pm 0.54$

We then applied our method to the Coma cluster (chapter 5). We analyzed the SDSS data of projected distances and velocities, up to 20 Mpc far from the Coma center. Our work led to the detection of six sheets in the environment of the cluster which carried to the following estimation of the Coma cluster mass:

- $M_v = (8.36 \pm 0.85) \cdot 10^{14} M_\odot$ for the usual cutting of the outskirts
- $M_v = (9.89 \pm 1.00) \cdot 10^{14} M_\odot$ for a slightly different division, in which the wedges are a little shifted.

These values are in agreement with previous results from other standard methods (chapter 2) based on the dynamical analysis of the cluster member galaxies (virial theorem method or Jeans equation), on the X-ray emission of the diffuse hot gas, or on effects like the gravitational lensing or the distortion of the CMB (SZE). We note however that our method tends to underestimate the Coma virial mass, compared to previous measurements which either assume equilibrium or sphericity.

The next step of this work should be to apply this method to a sample of clusters of galaxies, in order to make a statistical test on its efficiency. Moreover, this technique shows to have promising possible developments. For example, one could look at large distances from the cluster along the line of sight, instead of along the projected radius on the sky. This would mean to analyze galaxies within a larger redshift range around the cluster. Another useful analysis could be combining our mass estimation technique with different methods, such as the ones based on X-ray observations, gravitational lensing or SZE, since each method is biased in a different way. Using a combined analysis could help to reduce these biases and the errors on the masses, in order to reach a more accurate estimation.

Within this work, we also constrained the spatial orientation of the detected structures and tried to use it to deproject the orientation of galaxy clusters in the three-dimensional space. A first, qualitative approach showed that there is a correlation between the values of the mass returned by different sheets and their orientation with respect to the major or minor axes of a triaxial ellipsoidal halo. Therefore, another future perspective is to deepen the analysis we started (chapter 6) in order to test whether our method can actually be used as an effective tool to extract information about the three-dimensional shape and orientation of galaxy clusters.

Acknowledgements

I would like to say thank you

To my supervisor in Bologna, Lauro Moscardini, for always inspired me, for his advices and answers to my thousand questions, and for helped me despite the 1500 km of distance. And for being the reason I can write a program.

To my supervisor at Dark, Steen, for his brilliant ideas, his great patience, his friendly attitude and for all the help he gave me in this six months.

To Martina, my first landmark at Dark and in Copenhagen, for the professional and personal relationship we built in this few months, for being there whenever I needed her, for all the things that we did and (who knows?) we will do together.

To Dark Cosmology Centre for accepting me and have been a new small home to me, with its wonderful and cozy lounge and the irreplaceable italian (and not) community.

To Copenhagen, to gave me these incredible six months, unforgettable friends, Maria, Letizia, Chiara, Laura, Aldo, Naja, Fabio (all of them!), Alessandro, Karen, Joakim, Rikke, and for being a wonderful, special town that sometimes really reminded me of Bologna. I will miss you.

To my mum and dad, for growing me up, for let me always free to make my own choices, for being so similar to me in something and so different in other things, for being always an example and a certainty. To my whole family, for being with me and caring about me, from the Earth and beyond.

To Anna, Valeria and Francesca, for being for ten years a fixed point in my life, for being the people I know I can always rely on, despite everything.

To the Astrogirls, my crazy girls who kept me company in this long path, with their cheerful laughs and their wonderful way of being. To Matteo and Riccardo, loyal friends and really special guys, for the amazing days we spent and we will spend together. To Mario and Valeria for these two nice years we spent together, for the wine and the Japanese food, for our fantastic movie nights and their reliable friendship.

To Barbara, my strong and polyhedral teacher, for let me know her and the tissues and for the book we will write together.

To all my friends, from school, university, rhythmic gymnastics, aerial silks, trapeze, because the person I am is made by a small piece of every one of you.

To Cristina, Francesco and Elisa, for being my sweet, messy family, always. To Cri for the vital energy she conveys me, for the thousand special moments we lived together, for always treated me on par and for being my Plotinian One. To Fra for sharing my passion for science and for everything that is crazy and adventurous, for his annoying accent, for his brilliant mind. To Ely, for having always been my model and my support, for the fights and the experiences we shared together in a lifetime. To Alice and Manu for opened my mind and my heart and for gave me another reason to come back in Bologna.

To Matteo, always with me, even when I didn't know yet, for being there in these six months I wasn't, for the past almost four years and for the future ones.

To Bologna, my town, my house, my home. For its red bricks and its snug arcades, for the roads I walked on, for the ones I haven't discovered yet, for being simply wonderful.

Thanks to all of you
Elena

Ringraziamenti

Vorrei dire grazie

Al mio relatore a Bologna, Lauro Moscardini, per avermi sempre ispirata, per i suoi consigli e risposte alle mie mille domande, e per avermi aiutata nonostante i 1500 km di distanza. E per essere la ragione per cui so scrivere un programma.

Al mio supervisor al Dark, Steen Hansen, per le sue idee brillanti, la sua grande pazienza, il suo fare amichevole e per tutto l'aiuto che mi ha dato in questi sei mesi.

A Martina, il mio primo punto di riferimento al Dark e a Copenhagen, per il rapporto professionale e personale che abbiamo costruito in questi pochi mesi, per essere stata lì ogni volta che ne avevo bisogno, per tutte le cose che abbiamo fatto e che (chissà?) faremo insieme.

Al Dark Cosmology Centre per avermi accolta ed essere stato una nuova piccola casa per me, con la sua stupenda e accogliente sala e l'insostituibile comunità italiana (e non).

A Copenhagen per avermi dato questi incredibili sei mesi, amici indimenticabili, Maria, Letizia, Chiara, Laura, Aldo, Naja, Fabio (tutti quanti!), Alessandro, Karen, Joakim, Rikke, e per essere una città meravigliosa e unica che a volte mi ha davvero ricordato Bologna. Mi macherai.

A mia mamma e mio papà, per avermi cresciuta, per avermi sempre lasciata libera di fare le mie scelte, per essere così simili a me in alcune cose e così diversi in altre, per essere sempre un esempio ed una sicurezza. A tutta la mia famiglia per essere con me ed aver cura di me, dalla Terra e oltre.

Ad Anna, Valeria e Francesca, per essere da dieci anni un punto fermo nella mia vita, per essere le persone su cui so di poter sempre contare, nonostante tutto.

Alle Astrogirls, le mie pazze ragazze che mi hanno tenuto compagnia in questo lungo cammino, con le loro risate allegre ed il loro meraviglioso modo di essere. A Matteo e Riccardo, amici leali e ragazzi davvero speciali, per gli splendidi giorni che abbiamo passato e che passeremo insieme. A Mario e Valeria per questi due begli anni trascorsi insieme, per il vino ed il giapponese, per il nostro fantastico cineforum e per la loro amicizia affidabile.

A Barbara, la mia teacher forte e poliedrica, per avermi fatto conoscere lei e i tessuti e per il libro che scriveremo insieme.

A tutti i miei amici, da scuola, università, ginnastica ritmica, tessuti, trapezio, perché la persona che sono è fatta da un piccolo pezzo di ognuno di voi.

A Cristina, Francesco ed Elisa, per essere la mia dolce, caotica famiglia, sempre. A Cri per l'energia vitale che mi trasmette, per i mille momenti speciali che abbiamo vissuto insieme, per avermi sempre trattata alla pari e per essere il mio Uno Plotiniano. A Fra per la passione che condividiamo per la scienza e per qualunque cosa sia pazza e avventurosa, per il suo accento fastidioso, per la sua mente brillante. Ad Ely, per essere sempre stata per me un esempio e un supporto, per le litigate e le esperienze che abbiamo condiviso insieme in tutta una vita. Ad Alice e Manu, per aver aperto la mia mente e il mio cuore e per avermi dato una ragione in più per tornare a Bologna.

A Matteo, sempre con me, anche quando ancora non lo sapevo, per essere rimasto lì in questi sei mesi in cui io non c'ero, per gli scorsi quasi quattro anni e per quelli che verranno.

A Bologna, la mia città, la mia dimora, la mia casa. Per i suoi mattoncini rossi e i suoi portici accoglienti, per le strade che ho percorso, per quelle che non ho ancora scoperto, per essere semplicemente meravigliosa.

Grazie a tutti voi
Elena

Bibliography

- [1] S. W. Allen, A. E. Evrard, and A. B. Mantz. Cosmological Parameters from Observations of Galaxy Clusters. *ARA&A*, 49:409–470, September 2011.
- [2] M. Bartelmann and P. Schneider. Weak gravitational lensing. *Phys. Rep.*, 340:291–472, January 2001.
- [3] P. Bett, V. Eke, C. S. Frenk, A. Jenkins, J. Helly, and J. Navarro. The spin and shape of dark matter haloes in the Millennium simulation of a Λ cold dark matter universe. *MNRAS*, 376:215–232, March 2007.
- [4] B. Binggeli. The shape and orientation of clusters of galaxies. *A&A*, 107:338–349, March 1982.
- [5] J. Binney and G. A. Mamon. M/L and velocity anisotropy from observations of spherical galaxies, or must M87 have a massive black hole. *MNRAS*, 200:361–375, July 1982.
- [6] J. Binney and S. Tremaine. *Galactic Dynamics: (Second Edition)*. 2008.
- [7] S. Borgani. Cosmology with Clusters of Galaxies. In M. Plionis, O. López-Cruz, and D. Hughes, editors, *A Pan-Chromatic View of Clusters of Galaxies and the Large-Scale Structure*, volume 740 of *Lecture Notes in Physics*, Berlin Springer Verlag, page 287, 2008.
- [8] S. Borgani and L. Guzzo. X-ray clusters of galaxies as tracers of structure in the Universe. *Nature*, 409:39–45, January 2001.
- [9] J. E. Carlstrom, G. P. Holder, and E. D. Reese. Cosmology with the Sunyaev-Zel’dovich Effect. *ARA&A*, 40:643–680, 2002.
- [10] Sean M. Carroll. *Spacetime and Geometry: An introduction to General Relativity*. 2003.

- [11] D. Carter and N. Metcalfe. The morphology of clusters of galaxies. *MNRAS*, 191:325–337, May 1980.
- [12] A. Cimatti. *Galaxy Clusters*. 2007.
- [13] D. Coe. Dark Matter Halo Mass Profiles. *ArXiv e-prints*, May 2010.
- [14] P. Coles and F. Lucchin. *Cosmology: The Origin and Evolution of Cosmic Structure (Second Edition)*. 2002.
- [15] M. Colless, G. Dalton, S. Maddox, W. Sutherland, P. Norberg, S. Cole, J. Bland-Hawthorn, T. Bridges, R. Cannon, C. Collins, W. Couch, N. Cross, K. Deeley, R. De Propris, S. P. Driver, G. Efstathiou, R. S. Ellis, C. S. Frenk, K. Glazebrook, C. Jackson, O. Lahav, I. Lewis, S. Lumsden, D. Madgwick, J. A. Peacock, B. A. Peterson, I. Price, M. Seaborne, and K. Taylor. The 2dF Galaxy Redshift Survey: spectra and redshifts. *MNRAS*, 328:1039–1063, December 2001.
- [16] A. Diaferio. Mass estimation in the outer regions of galaxy clusters. *MNRAS*, 309:610–622, November 1999.
- [17] S. Ettori, A. C. Fabian, S. W. Allen, and R. M. Johnstone. Deep inside the core of Abell 1795: the Chandra view. *MNRAS*, 331:635–648, April 2002.
- [18] S. Ettori, P. Tozzi, and P. Rosati. Constraining the cosmological parameters with the gas mass fraction in local and $z < 0.7$ galaxy clusters. *A&A*, 398:879–890, February 2003.
- [19] A. E. Evrard, J. Bialek, M. Busha, M. White, S. Habib, K. Heitmann, M. Warren, E. Rasia, G. Tormen, L. Moscardini, C. Power, A. R. Jenkins, L. Gao, C. S. Frenk, V. Springel, S. D. M. White, and J. Diemand. Virial Scaling of Massive Dark Matter Halos: Why Clusters Prefer a High Normalization Cosmology. *ApJ*, 672:122–137, January 2008.
- [20] M. Falco, S. H. Hansen, R. Wojtak, T. Brinckmann, M. Lindholmer, and S. Pandolfi. A new method to measure the mass of galaxy clusters. *MNRAS*, 442:1887–1896, August 2014.
- [21] D. J. Fixsen. The Temperature of the Cosmic Microwave Background. *ApJ*, 707:916–920, December 2009.
- [22] B. Fort and Y. Mellier. Arc(let)s in clusters of galaxies. *A&A Rev.*, 5: 239–292, 1994.

- [23] L. Gao, J. F. Navarro, C. S. Frenk, A. Jenkins, V. Springel, and S. D. M. White. The Phoenix Project: the dark side of rich Galaxy clusters. *MNRAS*, 425:2169–2186, September 2012.
- [24] M. J. Geller, A. Diaferio, and M. J. Kurtz. The Mass Profile of the Coma Galaxy Cluster. *ApJ*, 517:L23–L26, May 1999.
- [25] M. Girardi, S. Borgani, G. Giuricin, F. Mardirossian, and M. Mezzetti. Optical Luminosities and Mass-to-Light Ratios of Nearby Galaxy Clusters. *ApJ*, 530:62–79, February 2000.
- [26] S. Gottloeber and A. Klypin. The ART of Cosmological Simulations. *ArXiv e-prints*, March 2008.
- [27] L. Grego, J. E. Carlstrom, E. D. Reese, G. P. Holder, W. L. Holzapfel, M. K. Joy, J. J. Mohr, and S. Patel. Galaxy Cluster Gas Mass Fractions from Sunyaev-Zeldovich Effect Measurements: Constraints on Ω_M . *ApJ*, 552:2–14, May 2001.
- [28] S. H. Hansen, S. Pastor, and D. V. Semikoz. First Measurement of Cluster Temperature Using the Thermal Sunyaev-Zel’dovich Effect. *ApJ*, 573:L69–L71, July 2002.
- [29] J. P. Hughes. The mass of the Coma Cluster - Combined X-ray and optical results. *ApJ*, 337:21–33, February 1989.
- [30] Y. P. Jing and Y. Suto. Triaxial Modeling of Halo Density Profiles with High-Resolution N-Body Simulations. *ApJ*, 574:538–553, August 2002.
- [31] S. M. Kent and J. E. Gunn. The dynamics of rich clusters of galaxies. I - The Coma cluster. *AJ*, 87:945–971, July 1982.
- [32] A. V. Kravtsov, A. A. Klypin, and A. M. Khokhlov. Adaptive Refinement Tree: A New High-Resolution N-Body Code for Cosmological Simulations. *ApJS*, 111:73–94, July 1997.
- [33] J. M. Kubo, A. Stebbins, J. Annis, I. P. Dell’Antonio, H. Lin, H. Khiabani, and J. A. Frieman. The Mass of the Coma Cluster from Weak Lensing in the Sloan Digital Sky Survey. *ApJ*, 671:1466–1470, December 2007.
- [34] E. T. Lau, A. V. Kravtsov, and D. Nagai. Residual Gas Motions in the Intracluster Medium and Bias in Hydrostatic Measurements of Mass Profiles of Clusters. *ApJ*, 705:1129–1138, November 2009.

- [35] E. T. Lau, D. Nagai, A. V. Kravtsov, A. Vikhlinin, and A. R. Zentner. Constraining Cluster Physics with the Shape of X-Ray Clusters: Comparison of Local X-Ray Clusters Versus Λ CDM Clusters. *ApJ*, 755:116, August 2012.
- [36] M. Limousin, A. Morandi, M. Sereno, M. Meneghetti, S. Ettori, M. Bartelmann, and T. Verdugo. The Three-Dimensional Shapes of Galaxy Clusters. *Space Sci. Rev.*, 177:155–194, August 2013.
- [37] E. L. Lokas and G. A. Mamon. Dark matter distribution in the Coma cluster from galaxy kinematics: breaking the mass-anisotropy degeneracy. *MNRAS*, 343:401–412, August 2003.
- [38] J. C. Mather, E. S. Cheng, R. E. Eplee, Jr., R. B. Isaacman, S. S. Meyer, R. A. Shafer, R. Weiss, E. L. Wright, C. L. Bennett, N. W. Boggess, E. Dwek, S. Gulkis, M. G. Hauser, M. Janssen, T. Kelsall, P. M. Lubin, S. H. Moseley, Jr., T. L. Murdock, R. F. Silverberg, G. F. Smoot, and D. T. Wilkinson. A preliminary measurement of the cosmic microwave background spectrum by the Cosmic Background Explorer (COBE) satellite. *ApJ*, 354:L37–L40, May 1990.
- [39] S. M. Molnar, I.-N. Chiu, K. Umetsu, P. Chen, N. Hearn, T. Broadhurst, G. Bryan, and C. Shang. Testing Strict Hydrostatic Equilibrium in Simulated Clusters of Galaxies: Implications for A1689. *ApJ*, 724:L1–L4, November 2010.
- [40] A. Morandi, M. Limousin, Y. Rephaeli, K. Umetsu, R. Barkana, T. Broadhurst, and H. Dahle. Triaxiality and non-thermal gas pressure in Abell 1689. *MNRAS*, 416:2567–2573, October 2011.
- [41] A. Morandi, M. Limousin, J. Sayers, S. R. Golwala, N. G. Czakon, E. Pierpaoli, E. Jullo, J. Richard, and S. Ameglio. X-ray, lensing and Sunyaev-Zel’dovich triaxial analysis of Abell 1835 out to R_{200} . *MNRAS*, 425:2069–2082, September 2012.
- [42] L. Moscardini, S. Matarrese, and H. J. Mo. Constraining cosmological parameters with the clustering properties of galaxy clusters in optical and X-ray bands. *MNRAS*, 327:422–434, October 2001.
- [43] J. F. Navarro, C. S. Frenk, and S. D. M. White. The Structure of Cold Dark Matter Halos. *ApJ*, 462:563, May 1996.
- [44] M. Oguri, M. B. Bayliss, H. Dahle, K. Sharon, M. D. Gladders, P. Natarajan, J. F. Hennawi, and B. P. Koester. Combined strong and

- weak lensing analysis of 28 clusters from the Sloan Giant Arcs Survey. *MNRAS*, 420:3213–3239, March 2012.
- [45] W. H. Press and P. Schechter. Formation of Galaxies and Clusters of Galaxies by Self-Similar Gravitational Condensation. *ApJ*, 187:425–438, February 1974.
- [46] P. Rosati, S. Borgani, and C. Norman. The Evolution of X-ray Clusters of Galaxies. *ARA&A*, 40:539–577, 2002.
- [47] G. Rossi, R. K. Sheth, and G. Tormen. Modelling the shapes of the largest gravitationally bound objects. *MNRAS*, 416:248–261, September 2011.
- [48] J. Sayers, S. R. Golwala, S. Ameglio, and E. Pierpaoli. Cluster Morphologies and Model-independent Y_{SZ} Estimates from Bolocam Sunyaev-Zel’dovich Images. *ApJ*, 728:39, February 2011. doi: 10.1088/0004-637X/728/1/39.
- [49] M. Sereno and A. Zitrin. Triaxial strong-lensing analysis of the $z_i0.5$ MACS clusters: the mass-concentration relation. *MNRAS*, 419:3280–3291, February 2012.
- [50] A. Skielboe, R. Wojtak, K. Pedersen, E. Rozo, and E. S. Rykoff. Spatial Anisotropy of Galaxy Kinematics in Sloan Digital Sky Survey Galaxy Clusters. *ApJ*, 758:L16, October 2012.
- [51] G. Soucail, B. Fort, Y. Mellier, and J. P. Picat. A blue ring-like structure, in the center of the A 370 cluster of galaxies. *A&A*, 172:L14–L16, January 1987.
- [52] D. N. Spergel, R. Bean, O. Doré, M. R. Nolta, C. L. Bennett, J. Dunkley, G. Hinshaw, N. Jarosik, E. Komatsu, L. Page, H. V. Peiris, L. Verde, M. Halpern, R. S. Hill, A. Kogut, M. Limon, S. S. Meyer, N. Odegard, G. S. Tucker, J. L. Weiland, E. Wollack, and E. L. Wright. Three-Year Wilkinson Microwave Anisotropy Probe (WMAP) Observations: Implications for Cosmology. *ApJS*, 170:377–408, June 2007.
- [53] R. A. Sunyaev and Y. B. Zeldovich. The Observations of Relic Radiation as a Test of the Nature of X-Ray Radiation from the Clusters of Galaxies. *Comments on Astrophysics and Space Physics*, 4:173, November 1972.
- [54] J. Svensmark, R. Wojtak, and S. H. Hansen. Effect of asphericity in caustic mass estimates of galaxy clusters. *ArXiv e-prints*, May 2014.

- [55] L. S. The and S. D. M. White. The mass of the Coma cluster. *AJ*, 92: 1248–1253, December 1986.
- [56] S. D. M. White, J. F. Navarro, A. E. Evrard, and C. S. Frenk. The baryon content of galaxy clusters: a challenge to cosmological orthodoxy. *Nature*, 366:429–433, December 1993.
- [57] R. Wojtak, E. L. Lokas, G. A. Mamon, S. Gottlöber, A. Klypin, and Y. Hoffman. The distribution function of dark matter in massive haloes. *MNRAS*, 388:815–828, August 2008.
- [58] F. Zwicky. Die Rotverschiebung von extragalaktischen Nebeln. *Helvetica Physica Acta*, 6:110–127, 1933.